Mitochondria: Bioenergetics and Predictive Therapeutics Using Vibrational Spectroscopy

by

Jason Solocinski

A dissertation submitted in partial fulfillment
of the requirements for the degree of
Doctor of Philosophy
(Mechanical Sciences and Engineering)
in the University of Michigan-Dearborn
2021

Doctoral Committee:

Nilay Chakraborty, BioNexus Foundation-ATCC, Chair
Professor Krisanu Bandyopadhyay
Associate Professor Gargi Ghosh
Professor Oleg Zikanov

Jason Solocinski

jsolocin@umich.edu

ORCID iD: 0000-0001-8292-2313

Dedication

I dedicate this work to everyone who, academically or otherwise, has supported me absolutely up to this point in my life. Firstly, my mother, Cindy Solocinski, who has allowed me to live in comfort and pursue education unencumbered by outside forces and without judgement. My sister, Kristy Solocinski, whose endearing nicknames have permeated space and time, to whom I am exceedingly grateful for. She won being the first doctor in the family, as well as best sister. Her unique creations bring much joy. My father, John Solocinski, to whom would always provide a nice time at the links or tables, with an immense range of conversations. My cousin, Michael Laurence, who among other things, fostered my greatest passion, which is exceptional culinary delights. My uncle, Gary Lesniewski, who reminds me that youth is relative, but pursuit of happiness is not. And the rest of my family, where I deem myself lucky compared to others, for their overall support, generosity, and kindness.

For friends, I must thank Matthew Bunch for our shared sense of humor, outlooks, and appreciation for many of the fine things in life. Eric Page, undoubtedly my oldest friend, with whom I could regale stories of good old times with forever. To Elizabeth, well, thank you for being a friend. My advisor, Nilay Chakraborty, whose mentorship, compassion, and selflessness have provided me with invaluable skills I doubt I would ever have acquired otherwise. I would not have made it to the finish without his unyielding support. I do not show emotion openly in general, but for anyone not addressed by name, it does not diminish my respect and appreciation; “Deeds will not be less valiant because they are unpraised.”

Acknowledgements

There are many people to which I owe thanks for support and collaboration along the way;

To members who have been in and out of my lab since I started; Quinn Osgood, Lukas Underwood, Eric Rosiek, and Mian Wang. They were always kind, supportive, and willing to lend a helping hand. My committee members, Drs. Oleg Zikanov, Gargi Ghosh, and Krisanu Bandyopadhyay for support and guidance on the final portion of my academic education. Dr. Michael Menze at the University of Louisville, along with his lab, has provided immense guidance and insights on many research projects together. His expertise in the biology domain is invaluable, particularly with respect to cell physiology. I hope to work with him in the future. Dr. Aloke Dutta, at Wayne State University for providing guidance and novel drugs for a portion of the research contained within. Dr. Michael Flickinger, formerly of North Carolina State University, and his lab for collaboration into several preservation studies. Dr. Steven Hand, for use of the *Afr*LEA3m protein in a portion of the research contained within. For the research and academic grants provided directly to me and indirectly via PIs, largely awarded by the National Science Foundation and the University of Michigan.

Table of Contents

List of Figures

Figure

Abstract

Biomedical research comprises one of the most importantt and well-funded areas in all of scientific research. Technological innovation is a relatively small component of all research overall, but the applications are of immense benefit. Incorporation of already existing technologies from other areas of research directly into a biomedical setting is a simple way to leverage human innovation into the highest applicability.

Vibrational spectroscopy is one such technology which, while steadily seeing more and more use in biomedical imaging, is still underutilized. Such advanced microspectroscopic techniques can leverage their ability to analyze global information in a cellular system to higher throughput and increased efficiencies.

Metabolism is a key global system for every cell type and organism. Energy production, metabolic pathway augmentation, metabolite analysis, and appraisal of overall metabolic poise are several ways in which characterization of metabolism can be used analytically. Each of these can provide valuable insights into cellular systems and associated conditions, namely illness and disease.

Using Raman spectroscopy to characterize metabolism has led to several interesting results. First, analysis of drug candidacy has shown a novel mode for drug testing. Effectively evaluating cellular health based on several different techniques shows level compatibility across the techniques employed. Localized spectroscopic analysis provides further evidence for

mitochondrial protection conferral. In a similar vein of research, targeted analysis of desiccation tolerant proteins, localized to mitochondria, likewise showed a protective mechanism. Finally, an analysis of substrate change directly on metabolism was carefully evaluated, with an outcome of visualizing effects of varying metabolic pathways upon overall global cellular metabolism.

These studies provide a strong platform for spectrometabolic evaluation to be considered for a variety of advanced characterization techniques. Coupling this method with other emerging technologies has the potential to shift the standards for metabolic evaluation.

Chapter 1

Introduction

The investment in biomedical research is the highest across all research and development sectors. Worldwide, this amounts to approximately $133 billion per year. (Grassano, 2020) The United States federal government, via the National Institute of Health, appropriates approximately $41.7 billion into this research, generally with increased allocation year-to-year. (Public Law 116-94, 2020) Domestic industry spends nearly $40 billion to this end. (Stewart, 2015) The development of a single drug from idea to market ranges from $314 million to $2.8 billion, the average cost being $985 million. (Wouters, 2020) Perhaps the most significant factor which contributes to the enormous costs of pharmaceuticals to market is the U.S. Food and Drug Administration approval process, which rejects some 86.2% of initial filings. (Wong, 2019) Even small improvements to research method optimization can decrease real costs tremendously.

Incorporating advanced techniques to achieve improved efficiency of research, both in terms of cost and time investment, is therefore a particularly desirable goal. By bridging traditional methods, which have widespread use and degree of confidence, with modern techniques, which have more attractive and useful features, a new paradigm of improved research techniques can be established. There are, of course, many different techniques which can be employed to bring about such broad changes.

Vibrational spectroscopy is a technique which uses intrinsic characteristics to supply global molecular information. The two primary forms of vibrational spectroscopy are Raman and Infrared. This can be used for widespread material analysis, such as the effects of corrosion on metals or the distribution of polymers in advanced composites. (Hayez, 2004; Tanaka, 2006) However, these techniques show particular utility in a biological setting on a cellular basis. (Gremlich, 2000) The unification of multiple traditional techniques into one systemic process should create much lower barriers to research where such global analysis would be of particular scientific interest.

One such global system that is universally studied and has profound implications for disease, ageing, and performance is metabolism. Metabolism is the totality of all process which occur to sustain life processes for a particular organism. Of principal interest is the biochemistry of how the body generates energy for these processes. Some of the most important, though certainly not exhaustive, metabolic pathways are oxidative phosphorylation, the electron transport chain, glycolysis, pentose phosphate pathway, and fatty acid biosynthesis. The first two occurring inside of the mitochondrial membrane, while the remainder takes place in the cytosol. Quantifying these chemical processes gives direct insight into the bioenergetics, metabolic poise, and potential cellular dysfunction. (Dagley, 1970)

One clear example where metabolism varies drastically is comparing primary cells, which are the cells or tissues which a patient or subject would provide, to model tumor derived cell lines, which are derived from primary cells that have mutated to grow beyond normal cellular senescence and so become immortalized, e.g., HeLa or HepG2 cells. (Scherer, 1953) These cell lines are very important to biomedical research due to their relative ease of use, cost effectiveness, and utility in being models for various research interest such as toxicity screening. However, these cells tend to

display a proclivity for alternate pathways of biosynthetic energy production. Namely, there is a distinct shift in upregulation for glycolytic flux so that substrate level phosphorylation occurs over the primary bioenergetic mode of primary cells, which lies in oxidative phosphorylation localized to the mitochondria and the associated electron transport chain. This favoring of glycolysis over aerobic respiration is known as the Warburg effect and is seen as a hallmark of most tumor derived cells (Warburg, 1956) So, by evaluating global metabolic poise, a cell can be determined whether to be of primary origin or tumor derived.

By being able to monitor metabolism via non-invasive spectroscopy as has been described, the individual cell response to targeted therapeutic treatments can be evaluated. It is possible to compartmentalize the cell into its constituent cellular features, such as nucleus, mitochondria, and cell membrane, via vibrational spectroscopy and so to see exactly where changes to the treatment are occurring. Furthermore, repetitions of treatments over long periods of time can be viewed per the same individual cell, so that statistical averaging of large cell numbers cannot miss intricacies inherent on a cell-to-cell basis. The ability to see a pharmaceuticals impact on metabolism in a physiological setting is the basis for developing a therapeutic method which would eventually lead to a clinical application. This would reduce sample waste and increase global cellular information availability which would have faster analytical turnarounds. The method proposed herein has the ability to make many therapeutics safer, more reliable, and have broader application. This would, in general, promote a more discerning analysis, especially with respect to the predictive appraisal of a drug based on metabolism and which patients would be most affected by a particular drug treatment.

Chapter 2

Characterization of Metabolism

2.1 Metabolism

Metabolism is fundamental to life in that it comprises all processes which allow an organism to function. Metabolism can be organized into several key purposes as the complexity of all biochemical processes is immense. Foremost, it considers the biochemistry associated with the conversion of energy sources into biologically available energy. There exist hundreds of metabolic pathways, though generally some are far more efficient and thus more common across all organisms. (Smith, 2004) One example being carboxylic acids necessary for the citric acid cycle which is found in all known organisms. Similarly, metabolism concerns input fuel being catabolized into base building blocks for common biomolecules such as lipids, proteins, and nucleic acids. It must also consider elimination of waste or byproducts of biochemical processes.

Evaluation of metabolism in humans can be used to detect certain metabolically linked diseases, namely type II diabetes, neurodegenerative diseases, and cancers, as normal metabolic function is severely impaired. Furthermore, many drug compounds will have an effect upon cellular metabolism, whether intended or not. They may be specifically designed to alter metabolism, (Wilkinson, 2005) but all too often this occurs as a result of unintended toxicity. (Gillette, 1974) In humans, this toxicity will predominately occur in the liver, as this organ is specifically responsible for metabolizing and eliminating toxins from the body. However, certain

drugs, or high enough levels of any drug compound, can overwhelm the liver and cause liver failure due to intracellular component injury, typically the mitochondria. Having the ability to characterize metabolism as a whole, and on subcellular level of mitochondria can lead to important insights into such diseases largely based upon drug-induced toxicity.

2.2 Mitochondria

Through genomic deduction (Anderson, 2003) and other evidence, (Gray, 2001; Melendez-Hevia, 1996) it is theorized that modern mitochondrial evolution has its origins possibly 2 billion years ago. Due to the high degree of shared genetic code shared between mitochondria and α-proteobacteria, it is also surmised that bacteria became endosymbionts for another primitive prokaryotic cell type. This may have been caused due to extreme global events which dramatically increased the atmospheric oxygen availability. (Smith, 2018) Since oxygen is a powerful oxidizing agent, it acts as a strong toxin for anaerobic organisms. Therefore, there was an evolutionary incentive to incorporate the aerobic-respiration-capable α-proteobacteria. This became a powerful feature, in that excess chemical energy in the form of adenosine triphosphate (ATP) was generated. It is possible that this eventually led to the rise of not only eukaryotic cells, but all complex multicellular life, which reaches into today's genetics.

Today, mitochondria are present in nearly all eukaryotic cells, with small exceptions such as red blood cells. An important structural feature to the organelle is that it is bound by a phospholipid bilayer, embedded with many proteins called porins. Mitochondria are responsible for regulating many metabolic pathways. In aerobic environments, mitochondrial respiration via oxidative phosphorylation accounts for the dominant pathway for energy production across most

cell types. In anaerobic environments, this largely shifts to fermentation, producing lactate. While fermentation has faster rates of ATP production than respiration, the overall net yield of ATP favors respiration by 15-to-1 (mol ATP per mol glucose). (Bonora, 2012) There are certain cell types which do not display this standard preferred respiration-based metabolism. As previously discussed, cancers generally prefer substrate linked phosphorylation, meaning that other pathways, such as glycolysis or the pentose phosphate pathway (PPP) are utilized much more, regardless of aerobic conditions. (Vander Heiden, 2017)

Characterizing the metabolites, the biochemical molecules which serve as intermediates for metabolic processes such as ATP and ADP (adenosine di-phosphate), has been of immense interest to research for decades. The evaluation of all metabolites in a cellular system is called metabolomics and can be used as a basis for metabolism linked research, especially in the novel pharmaceuticals field.

2.3 Extracellular Flux Analysis

Bioenergetic monitoring can be achieved using extracellular flux analysis. Considered a "gold standard", this is a fluorescent probe technique which quantifies dissolved oxygen and proton concentrations in media contained within a transient microchamber. Both oxygen consumption rate (OCR) and extracellular acidification rate (ECAR) measurements are taken with respect to time and can be used to generate metabolic profiles, which can define the cellular metabolic regime. The method generally utilizes metabolism-altering reagents to characterize the full standard metabolic profile.

Oligomycin is a F_0F_1-ATPase inhibitor, (Capaldi, 2002) which causes respiration-linked ATP production to cease. Carbonyl-cyanide-4-(trifluoromethoxy) phenylhydrazone (FCCP) acts as the uncoupling agent which collapses the mitochondrial proton gradient and so uncouples oxidation from phosphorylation, maximizing OCR. Contributions to OCR due to non-mitochondrial processes is analyzed by applying both rotenone and antimycin A, which inhibit complex I and complex III of the mitochondrial membrane respectively, effectively eliminating all contributions to OCR via mitochondrial respiration.

Glucose can be supplied as to fully saturate basal ECAR. As previously stated, since oligomycin inhibits ATP synthase, and since the proton production from mitochondrial respiration does not then have upstream offset to ECAR, the effect is seen as a maximization of ECAR. 2-DG is a glucose analog which competitively inhibits hexokinase, effectively arresting glycolysis and so stopping glycolytic-linked change to ECAR.

2.4 Metabolomics

The Scripps Research Institute hosts a metabolite database containing some 450,000 entries. (Smith 2005) The Human Metabolome Database displays some 110,000 metabolites on record. (https://www.genome.jp/kegg/pathway/map/map01100.html) Of all known reposited biomolecules, generally about 300 are considered to be of most common relevance. Among these, only a handful are usually characterized, as these are metabolites directly linked with the most commonly used metabolic pathways, i.e., glycolysis, oxidative phosphorylation, PPP. There are many techniques available to analyze metabolites, to varying degrees of efficacy and limitations.

2.4a Mass Spectroscopy

Mass spectroscopy (MS) is a widely used analytical technique used in many fields. It possesses a very high degree of detection threshold and can identify virtually all compounds. (Sparkman, 2000) These devices consist of an ion source, a mass analyzer, and a detection system. They operate on the basis of measuring an ions mass to charge ratio. A sample enters the ionization field, e.g., an electron beam, where it is ionized. Due to the magnetic field in the analyzer portion, there is an induced deflection to the generated ionic particles which corresponds directly to the mass to charge ratio, which when processed after collection, can be used to exactly show weight distributions of the sample in a spectrum output which can be correlated to known molecules.

Mass spectroscopy is generally utilized in conjunction with either (high performance) liquid chromatography (LC) or gas chromatography (GC). Both of these chromatography techniques are highly effective in separating samples. (Sparkman, 2011) High performance liquid chromatography relies on passing a liquid sample in mobile phase through a filtering column filled with adsorbent of varying sized particles. The mass transfer effects of the high-pressure liquid sample input causes the sample to interact with the column based on sample particle size. This allows for the sample to be separated very accurately based on size, which increases sensitivity in the mass spectrometer. Gas chromatography is a technique which involves heating samples to vaporize, along with using another inert carrier gas to bring the vaporized sample in mobile phase to pass through the stationary phase where the sample can be detected through electronic detectors. In part, the ability to separate comes from the material properties of the analyte fluid, namely the vaporization point and adsorptive properties due to particle size, visualized as retention time.

Advantages of GC-MS are the very high separation reproducibility, compatibility with fluids, and relatively good sensitivity. Advantages of LC-MS are the flexibility of the technique,

accommodating to solids and liquids, and extremely high degree of detection sensitivity. However, both of these techniques are destructive (the sample is irrecoverable), requires relatively high amounts of sample (10-200 μL) and are slow analysis techniques.

2.4b Nuclear Magnetic Resonance Spectroscopy

Nuclear magnetic resonance (NMR) spectroscopy is a technique which fundamentally observes local magnetic fields around NMR-active atomic nuclei (most commonly H_1 and C_{13}). (Hoult, 1997) It works by inducing, via a magnetic field, a polarization of magnetic nuclear spins. The polarization is disturbed by a radio frequency pulse, which generates a weak oscillating magnetic field. The NMR-active nuclei emit electromagnetic waves which are detectable. NMR spectroscopy provides extremely high degrees of detection with unique signatures for a wide range of sample types. Spectral acquisition time increases directly with increase to element weight due to increased relaxation times, meaning samples can take minutes to hours to complete. Therefore, it has mixed utility when analyzing biological components, as many organic compounds are out of range for efficient scanning. Furthermore, NMR has very high costs (up to $5 million) and requires a relatively large amount of high purity sample.

Chapter 3

Raman Spectroscopy

3.1 Raman Scattering Theory

The chemical bonds between atom pairs can be modeled as a spring between point masses following Hook's Law, which represent a harmonic oscillator with a single resonant vibrational frequency. (Sasic, 2011) For molecules containing more than two atoms, normal vibrations occur at a total, for a molecule of n atoms, of 3n-5 for linear molecules and 3n-6 for nonlinear molecules. It is possible for different vibration modes to occur at the same frequency, and thus overlap. Furthermore, parts of molecules which are not coupled vibrationally to the rest of the molecule possess nearly the same frequencies of vibration, regardless of what molecules they are attached to. For example, a phenyl ring or thiol group will accord to the same vibrational signature no matter what it happens to be bound with. Vibrations are often grouped by the type of motion which occurs during oscillation. Some of these are; when bond length oscillates, it is termed "stretch", bond angle oscillation is termed "bend", while other specialized oscillations are "rock", "breathing", and "wag".

Raman scattering occurs when a photon has an inelastic collision with a molecule, which causes a quantized transfer of energy to the molecule. Graphing the intensity of the scattered photon relative to the energy shift from the incident light (meaning any electromagnetic wave, though typically in visible range) yields a Raman spectrum. The photon interaction with the

molecule excites the molecule to a virtual state, via an electrical distortion of the chemical bond by the lights electric field. This virtual state does not represent a quantum mechanical stationary state but rather an induced dipole moment. The virtual state instantaneously relaxes back to the ground state of the molecule, emitting a photon. If the photon is elastically scattered, whereby the same vibrational state is achieved after emission, Rayleigh scattering has occurred. If the photon inelastically loses energy, thereby reducing frequency and increasing wavelength, a Raman-Stokes shift has occurred. A photon which increases its vibrational energy and so has a decrease in wavelength is a Raman-Anti-Stokes shift.

Based on a quantum mechanical model (Placzek, 1959), an analytic equation can be written for Raman intensity;

$$I_R = (I_L \sigma_R X) PC$$

where I_R is Raman intensity [photons/sec], I_L is the intensity of the laser [photons/sec], σ_R represents absolute Raman cross section [cm^2/molecule], X is an experimentally derived constant, P is sample path length [cm], and C is concentration [molecules/cm^3].

This shows several practical considerations for spectral acquisition. Since Raman intensity is proportional to excitation intensity, Raman signal can be improved simply by increasing laser power, up until the threshold level where the intensity may damage the analyte. Lasers are used due to the feature of coherence (spatial and temporal), that is, all light is in the same phase; monochromatic and collimated. Without this feature, it would be near impossible to analyze the scattered light. Furthermore, intensity is directly proportional to the scattering molecules of the

analyte, which allows for quantitative analysis. Raman intensity increases with Raman photon frequency (to the fourth power) and since Raman photon frequency is directly proportionate to the excitation frequency, the Raman intensity greatly increases with increasing energy level corresponding to the type of electromagnetic wave.

3.2 Raman Microspectroscopy with Common Techniques

Coupling a Raman spectrometer to a microscope system has several attractive features. The basic schematic of such a system is shown below. Raman requires very little sample preparation due to the nature of the scattering event. Spectra can be acquired from very small sample sizes. Raman is generally insensitive to water and so can be used where many other techniques, including IR spectroscopy, are disadvantaged. Using pinhole optics, a confocal microscopic configuration can be employed, which further allows raster imaging. This also allows for the generation of hyperspectral maps by taking large arrays of individual Raman spectra and then comparing a spectral feature based on intensity to map the specific peak position across the area of the array scan.

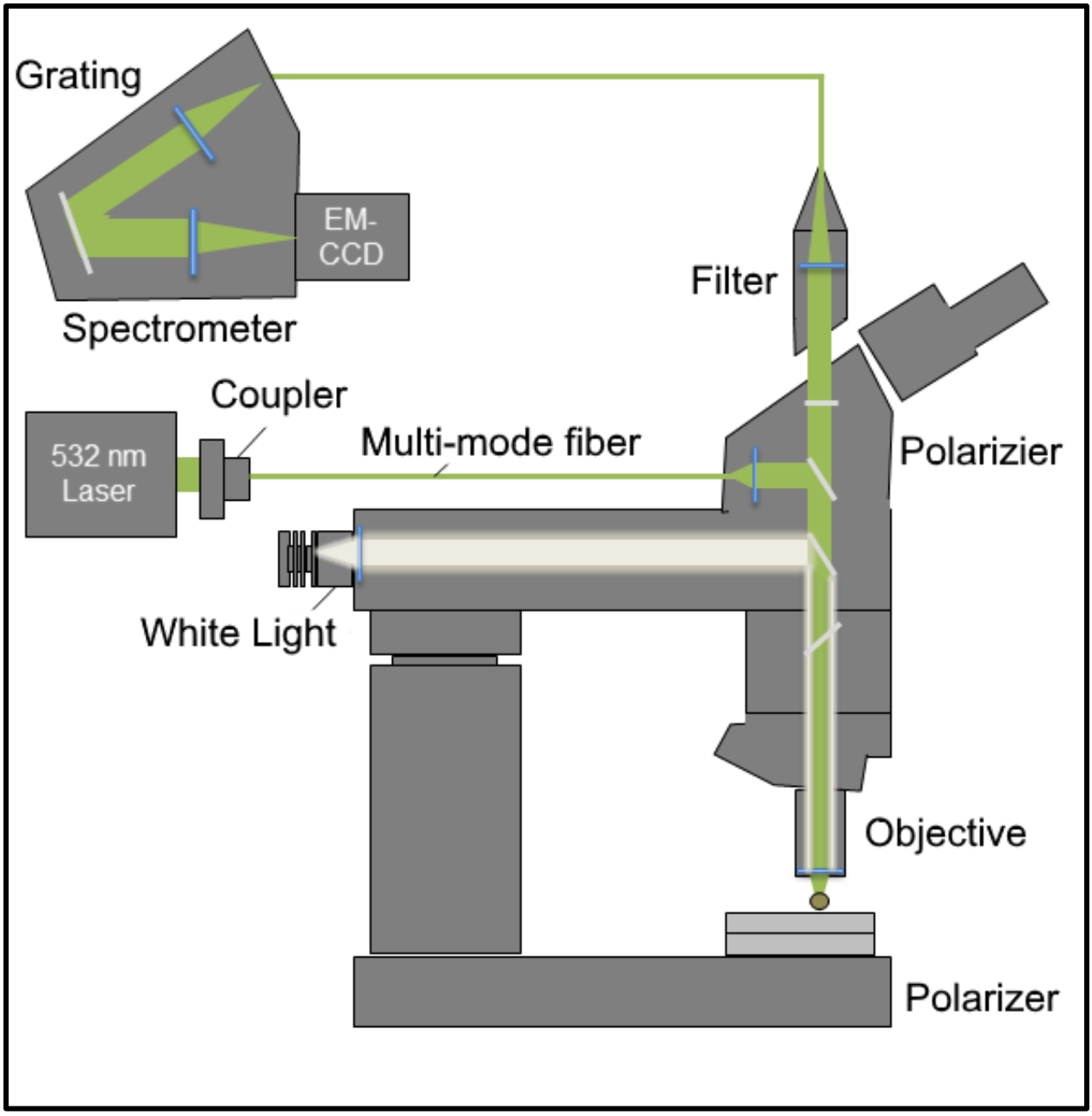

Figure 3.1: Schematic of Raman spectrometer connected to microscope

Figure 3.1 shows the three primary components of a microspectroscopic system; the microscope, the light source, and the spectrometer with detector. The microscope is coupled, via a multi-mode cable, to the laser excitation source, a Nd:YAG (neodymium-doped yttrium

aluminum garnet) laser which is frequency doubled to emit at 532 nm wavelength. The laser is directed though a polarizer and then the microscope objective to the sample where scattering occurs from the analyte. The scattered light is collected with the same objective and travels through the microscope, where it is filtered by a notch, line, or long pass filter to eliminate or reduce the Rayleigh scattered light. The light also will travel through a pinhole optic to create the confocal configuration. Upon entering the spectrometer, the light will be expanded and focused onto the grating, an optical tool used to differentiate the beam of light based on wavelength due to the blazed surface (here either 600 or 1800 lines/mm). The beam is then condensed and strikes the detector. Here, an (EM)CCD is used, an electron multiplied charge couple device. Fundamentally, a CCD translates incident photons into electric charges. (Boyle, 1970) This allows the beam of wavelength-segregated light to be converted into an electronic based spectrum.

The quality of spectrum is generally characterized by the noise levels over the actual sensitivity, by the signal-to-noise (STN) ratio. There are many ways to improve this ratio; physically, materially, and mathematically. As previously stated, the laser power can be increased, up until damage thresholds are reached. The sample acquisition/integration time can be increased to lower non-Raman spectral contributions. Multiple accumulations can be acquired, whereby the averaging of spectra will cancel statistically random noise. One of the largest factors to negatively impact Raman spectrum output is fluorescence. This can be negated by using a different excitation wavelength outside of the fluorophore's excitation band. Alternatively, photobleaching techniques can be used. Materially, certain physical effects can be leveraged to produce a higher than nominal Raman scattering event probability (which randomly is approximately 1 in 10^{10} photons). This includes resonance Raman, surface enhanced Raman, and coherent anti-stokes Raman. Once the spectrum is acquired, mathematical tools can be used to reduce noise, improving STN ratio. This

includes the multivariate statistical methods of principal component analysis and cluster analysis. Finally, to separate spectral peaks which happen to overlap, deconvolution methods can be used.

3.2a Surface Enhanced Raman (SERS)

Surface enhanced Raman spectroscopy can be utilized when an analyte is very close to a metal surface. (Stiles, 2008) An electromagnetic enhancement occurs which serves to amplify the Raman intensity due to localized surface plasmons. Surface plasmons occur when an incident electrical field displaces the metal conducting electrons, causing an oscillating resonance which then has a charge transfer mechanism back to the analyte. Surface plasmons depend heavily upon surface topology. Smooth and flat surfaces are incapable of producing such an effect. But rough or colloidal metal, or specially nanostructured materials, generally made of silver or gold as these resonate with visible light frequencies, can produce increased Raman intensity output by a factor of 10^4 to an enormous 10^{14} improvement, depending on shape and other surface interaction variables.

3.2b Resonance Raman

Resonance Raman scattering occurs when the excitation radiation's photon energy level matches exactly the electronic absorption band, causing the Raman intensity to increase by as much as six orders of magnitude. (Robert, 2009) The falloff in Raman intensity is drastic as the resonance frequency is departed from. Thus, this technique only effectively works when a known laser emission wavelength happens to be the proper exciting wavelength for a molecule. This is generally difficult to accomplish. However, it has the obvious advantage of much improved signal

intensity. It can also be employed to characterize vibrational modes of a subgroup of molecules from a very large molecule, such as a polypeptide.

3.2c Coherent Anti-Stokes Raman (CARS)

Coherent anti-stokes Raman spectroscopy is a non-spontaneous technique used to increase Raman intensity. (Begley, 1974) The technique works by utilizing two laser beams to stimulate the analyte. One laser light (pump field) excites the molecules to an elevated virtual energy state. The second laser (Stokes field) scatters the already stimulated photon to an excited vibrational energy level. Light from the pump field excites this elevated vibrational energy state to another virtual energy level, before it sinks back to ground state, thereby emitting an anti-Stokes scattered photon.

3.3 Signal Processing

Basic signal processing methods are used to remove unwanted or non-Raman contributions from the resultant spectrum output after acquisition. While shielded from virtually all environmental influence, the CCD can still register cosmic rays. These are some of the most energetic particles that move throughout the universe, originating largely from supernovae of massive stars. These are relatively rare and easily subtractable. Every spectrum has a baseline saturation value which has many contributions, including thermal energy to the CCD, which is why it is typically stabilized to -60°C. The method used for baseline subtraction varies from sample to sample, usually dependent on if any fluorescence is acquired. Contributions from matrix or substrate components (aqueous environment or the slide an analyte rests upon), can generally

be removed by collecting pure spectrum of the contributing matrix and calculating a normalized subtraction.

3.3a Principal Component Analysis

Principal component analysis (PCA) is a mathematical technique which ultimately reduces the dimensionality of a (generally large) data set. (Wold, 1987) In general, PCA will only apply to hyperspectral maps, collected from large areas of a sample, with many spectra in the dataset. First, the data is standardized to z scores. A covariance matrix of p x p dimensions (where p is original dimensionality) is created and then reduced to lower triangular form. From here, eigenvalues and eigenvectors are computed and then ranked to determine what the principal components (PC) of the new reorganized dataset will be. Practically, the number of PCs to be included in the reconstructed data set is determined by a cutoff STN threshold, where real Raman signal is fully retained but noise is removed. This is because the actual Raman intensity is contained within the first few PCs, while the remainder PCs are only noise contributions. As an example, the original dimensionality is determined by the pixels on the CCD detector chip, which is 1600. PCA reduces the dimensionality from 1600 to approximately 10, where the remainder 1590 contain noise. This technique provides the best post processing reduction to noise, while preserving information. It is potentially liable to remove certain real Raman contributions, especially if the original sampled array does not contain proper distribution of all real Raman elements.

3.3b Cluster Analysis

Cluster analysis is premised on the simple notion of clustering sets of objects from a total population into groups based on the relative affinity the objects have to one another. (Edwards, 1965) How this is of benefit to Raman spectroscopy is in applying the model (here a centroid-based clustering model) to a hyperspectral image. The clustering engine will segregate individual data members into groups based on closeness to a central vector, generated by the total population information, as well as the predetermined number of clusters that are meant to be differentiated into. Practically, this can use a clustering algorithm (there are many) to separate a hyperspectral image into its primary features, e.g., for a cell, into the cell and surrounding water/media.

3.3c Deconvolution Analysis

Spectral deconvolution is the inverse process of convolution. It is a fundamental method used in spectroscopy. (Ayers, 1988) When spectral peaks, which present as Gaussian curves (or other normally distributed function), overlap in a single spectrum, as is common in the output from the CCD, then deconvolution must be employed to separate individual components from one another. The process by which this is done can be called non-linear iterative curve fitting, whereby an initial "best estimate" is made by either manual input or algorithmic recommendation, usually on the basis of analytical features such as 2^{nd} derivative analysis of spectrum. From deconvolution, analysis on individual peaks can take place on key properties such as peak intensity, peak position, peak width (usually taken at FWHM, full width at half maximum), and peak area, relative to baseline.

Chapter 4

Metabolic and Vibrational Spectroscopic Appraisal of the Protective Role of D-512 on Induced Neurodegenerative ROS Generation in PC12 Cells

4.1 Introduction

Parkinson's disease (PD) is a debilitating neurodegenerative disorder which largely affects the elderly population. Clinically, it is characterized by tremors, bradykinesia, rigidity, and postural instability, (Carlsson, 1959; Parkinson 2002) all of which are severe motor function impairments which is identic to PD. Principal symptoms are the effects of the loss of particular dopaminergic neurons of the substantia nigra pars compacta. (Bertler, 1959; Barbeau 1962) The result of this cellular loss being increased iron concentrations, acute changes in oxidative stress markers, and accumulation of 'Lewy bodies'. (Jellinger, 1992; Forno, 1996) Aging, toxicity, and mutation only account for 5% of PD cases. (Hornykiewicz, 1989; Langston, 1983; Schapira, 1993; Polymeropoulos, 1997; Lesage, 2009)

Creation of, or inability to detoxify, destructive free radicals and hydrogen peroxide (reactive oxygen species; ROS) in critical regions of the brain induce neuropathology of the common sporadic form of PD. Mitochondria are the organelles which have the ability to facilitate the most ROS generation, at levels upward of 90%. Toxins which inhibit mitochondrial complex I, such as rotenone, lead to defects in the electron transport chain (ETC) leading to leaked protons and energy deficiency. This proton leak can directly lead to ROS generation. Selective

vulnerability of dopaminergic neurons implies dopamine (DA) itself as a significant contributing factor to the disease genesis and progression. Autooxidation and metabolism of monoamine oxidase B can generate 6-hydroxydopamine (6-OHDA) and DA quinones, leading to higher ROS generation. (Linert, 2000)

The creation of a dopamine D2/D3 agonist compound, D-512, has been previously reported. (Shah, 2014) It has multi-faceted clinical application, as it acts as antioxidant, iron-chelator, and neuroprotector. (Li, 2010; Gogoi, 2011; Johnson, 2012) The findings of the initial study were shown to inhibit ROS generation in a mammalian neural model and ward against disease initiation and progression.

The metabolic implications and underpinnings of the novel D2/D3 agonists were not fully elucidated, however. To monitor the effects of clinically mirrored incubation conditions via extracellular flux analysis and Raman spectroscopy has given important insights into the effects of the mechanisms of D-512, used in a protective role against 6-OHDA induced ROS generation. Results herein show strong support for the use of D-512, as the in vitro cell model showed significantly diminished results where the neuroprotector was not employed.

4.2 Materials and Methods

4.2a Cell Culture and Treatments

Rattus norvegicus adrenal gland pheochromocytoma cells (PC12, ATCC CRL-1721) were cultured in T-25 flasks (Thermo Fisher Scientific, Waltham, MA) with RPMI 1640 (Gibco, Waltham, MA) medium supplemented with 10% heat-inactivated horse serum (Gibco, Waltham, MA), 5% fetal bovine serum (Gibco, Waltham, MA), 100 U/mL penicillin, and 100 ug/mL streptomycin in humidified air and 5% CO_2. Stock solutions of 6-OHDA, shown in fig. 4.1a, and D-512, shown in fig. 4.1b, were prepared in DMSO and aliquots were stored at −20°C and −80°C, respectively. The five treatment conditions are diagramed in fig. 4.1c and are as follows: 1) untreated cells, 2) 10 μM D-512 for 24 hr, 3) 75 μM 6-OHDA for 24 hr, 4) 10 μM D-512 for 24 hr followed by 75 μM 6-OHDA for 24 hr (pre-incubation), and 5) 10 μM D-512 for 24 hr followed by 10 uM D-512 and 75 μM 6-OHDA for 24 hr (pre/co-incubation) (Shah, 2014).

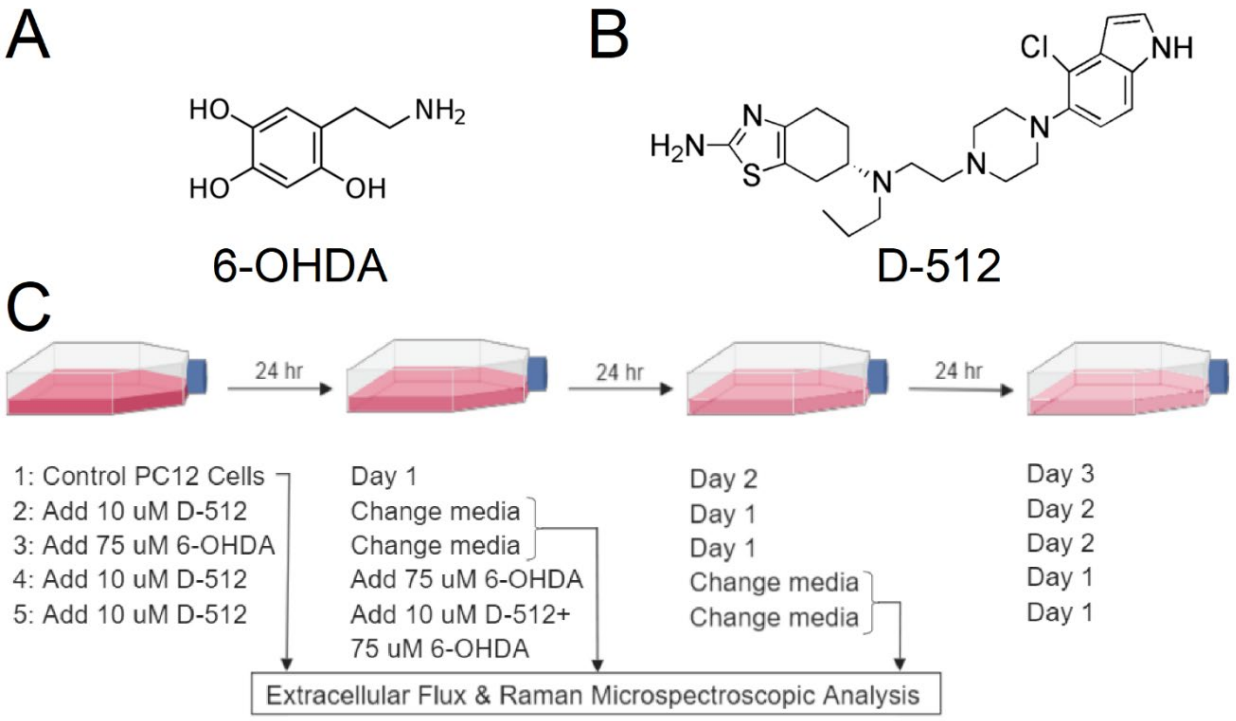

Figure 4.1: Molecular structure of reagents and treatment growth plan - A) Molecular structure of hydroxydopamine. B) Molecular structure of D-512. C) PC12 cells were incubated in five different conditions and then returned to normal culture conditions to view growth or else taken to extracellular flux or Raman spectroscopic analysis.

4.2b Metabolic Analysis

An extracellular flux analyzer (XFp Seahorse, Agilent Technologies, Santa Clara, CA) was used to characterize metabolic activity of PC12 cells. All Seahorse XFp consumables were purchased from Agilent. Cells were dissociated from culture flasks using trypsin (Gibco, Waltham, MA). The cells were centrifuged at 200 x g for 5 min, the supernatant was removed, and the cell pellet resuspended in media. Cell number was enumerated using a 0.04% trypan blue exclusion dye (Life technologies, Carlsbad, CA) and a hemocytometer (Hausser Scientific, Horsham, PA). Cells were placed in prescribed microwell plates at a seeding density of 10^4 cells

per well. After an initial 24 hr incubation to promote attachment, media was replaced with media solutions according to the previous five conditions for appropriate durations.

Both oxygen consumption rate (OCR) and extracellular acidification rate (ECAR) measurements were taken using standard Seahorse protocol, following optimization for cell line. Briefly, XFp cartridge sensors were hydrated, and injection ports loaded by the following; mitochondrial test reagents used oligomycin (1 μM), carbonyl-cyanide-4-(trifluoromethoxy) phenylhydrazone (FCCP, 0.5 μM), and rotenone/antimycin A (0.5 μM). Glycolysis test reagents used D-glucose (10 mM), oligomycin (1 μM), and 2-deoxyglucose (2-DG, 50 mM). All reagents have corresponding final well concentrations immediately after being listed.

Oligomycin is a F_0F_1-ATPase inhibitor, stopping respiration-linked ATP production. FCCP acts as an uncoupling agent that collapses the mitochondrial proton gradient and thereby uncouples oxidation from phosphorylation, maximizing OCR. The contribution to OCR via non-mitochondrial processes was measured using rotenone and antimycin A. Rotenone inhibits complex I and antimycin A inhibits complex III of the mitochondrial membrane, effectively arresting mitochondrial respiration.

Glucose was supplied as to fully saturate basal ECAR. As previously stated, since oligomycin inhibits ATP synthase, proton production from mitochondrial respiration does not offset ECAR, having an effect to maximize ECAR. 2-DG is a glucose analog which competitively inhibits hexokinase, effectively arresting glycolysis.

4.2c Measurement of Cell Viability

One week growth of all conditions was evaluated to determine the effect of D-512 and 6-OHDA on cell growth. PC12 cells were seeded in T-25 flasks at an initial cell number of $2.5x10^6$ in triplicate. These cells then had each of the treatment conditions applied for the allotted timeframes, shown in fig. 4.1c. After treatment concluded, the media was replaced (without D-512 or 6-OHDA) and left to culture for a further 24 hr (at which point they are considered to be at day 1). Cells were collected, as before, on day 1, 3, and 7 for independent flasks, which were grown in parallel such that counting would not disrupt further growth.

4.2d Raman Microspectroscopy

Spatially correlated Raman microspectroscopic measurements were employed to characterize living PC12 cell samples at in vitro culture conditions. A customized confocal microscope (Zeiss Corp., Germany) and Raman spectrometer combination (UHTS 300, WITec Instruments Corp., Germany) was used and the Raman spectra were collected using a sensitive CCD camera (Andor Technology, UK) at a spatial resolution of 500 nm. A 532 nm solid state laser calibrated to 20 mW was used for excitation and a custom 50X high resolution objective (Mitutoyo, Japan). The changes in the spectral signature from the intracellular space were analyzed using a hyperspectral molecular analysis technique. Spectral arrays were collected using a spatial dimension of 40μm×40μm with a spectral dimension of 80x80 pixels, with N=3. Each array of scans was collected using an integration time of 0.5 s. Typical background and substrate subtractions were employed, using WITec Project 5 and Peakfit v4 software. Principal component analysis (PCA) was used to reduce the dimensionality of the collected spectral data arrays into principal components (PCs) and then reconstructed according to a signal-to-noise threshold for

selecting PC number. Following noise reduction using PCA, hierarchal cluster analysis was used to construct average spectral signatures for regional components of the cellular hyperspectral arrays. Pure samples of 6-OHDA and D-512 were also acquired using point scanning to acquire base references for each compound when in solution (Fig. 4.8).

4.2e Statistical Analysis

Data are expressed as mean value ± standard error mean (SEM), unless otherwise noted. For multiple groups, statistical significance was determined using one-way analysis of variance (ANOVA). In all cases $p \leq 0.05$ was considered as statistically significant. Origin 2018 (OriginLab, Northampton, MA) was used for statistical analysis and graphical representation.

4.3 Results

4.3a Cellular Growth

Fig. 4.2a shows the normalized growth rates of PC12 cells in five conditions. Counts were performed on days 0, 1, 3, and 7. Initial cell density was equal across all samples at day 0. The latter counts were all normalized to their respective day 1 cell number.

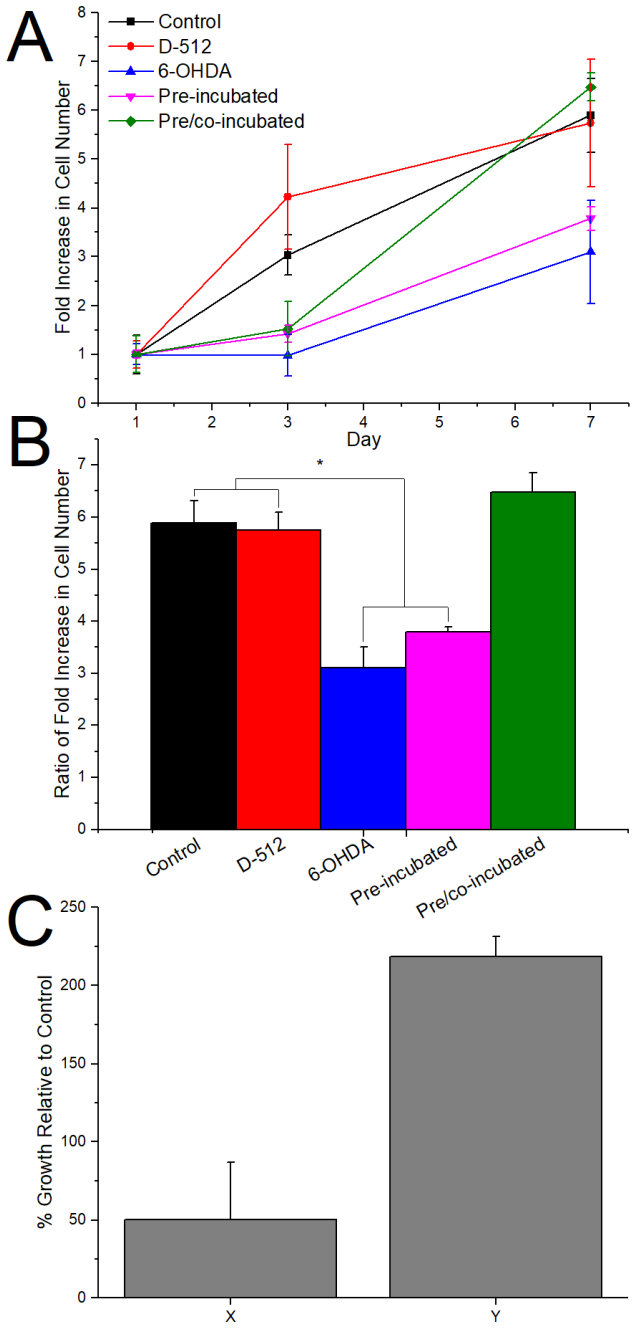

Figure 4.2: Growth rate comparison of several PC12 conditions - A) Cells were enumerated on days 1, 3, and 7. Most notable is the low early growth rate of the pre/co-incubated cells, followed by a rapid increase in cell number. B) Ratio of day 7 to day 1 counts, where overall impact of conditions is seen. D-512 and pre/co-incubated cells had no difference in growth rate compared to untreated cells. Conditions which were exposed to 6-OHDA without D-512 co-incubation had significantly lower growth levels than control. C) Pre/co-incubation cells had interesting growth characteristics, and so the growth rate from day 1 to day 3 (X) and from day 3 to day 7 (Y) were compared to control. There is a marked increase in growth rate from pre-day 3 to post-day 3. *$p<0.05$ against control. Error is +/- SEM, n=4

Fig. 4.2b displays the ratio of cell number from day 7 to day 1, highlighting one-week total growth for all conditions, shown as (mean ± SEM), n=4. Those cells which were grown without treatment, labeled control, (5.89 ± 0.41) and those treated with D-512 alone (5.74 ± 0.36) had very similar growth rates, higher than other conditions. D-512 cells had a higher initial growth (day 1 to 3) however. Cells treated with 6-OHDA (3.10 ± 0.40), including those with a pre-treatment of D-512 (3.79 ± 0.10), showed relatively poor growth (significance shown in fig. 4.2b). The cell counts were much decreased from day 0 to day 1, possibly indicating certain cells had better resistance to 6-OHDA and so did not all immediately perish. Cells which had D-512 in culture when 6-OHDA was applied had initially low growth, similar to the 6-OHDA alone condition, but followed by large increase in growth rate to compare to control cells (6.48 ± 0.37). This is shown clearly in fig. 4.2c, where X is the percent ratio of cell increase from day 1 to 3 (50.3%) and Y is the increase in day 3 to 7 (218.5%); both with respect to control growth.

4.3b Bioenergetics

Extracellular flux analysis for OCR, normalized to 10^6 cells, is shown in fig. 4.3a. Figure legend in top right indicates condition for A-D. Control cells have highest normalized basal OCR. Both D-512 and pre/co-incubated cells had lower OCRs by one-third fold. Both cell groups which had 6-OHDA incubation had significantly lower basal OCR than control. Oligomycin has the anticipated decreasing effect on OCR, across all cell groups. FCCP injection shows much increased OCR for control, D-512, and pre/co-incubation, approximately 30% over basal OCR. There was little increase for both 6-OHDA groups, indicating some critical injury to mitochondria of these cells as the oxidation-phosphorylation decoupling should be dependent only on total

mitochondria number. Rotenone injection inhibits all mitochondrial respiration and is therefore used as a zeroing metric.

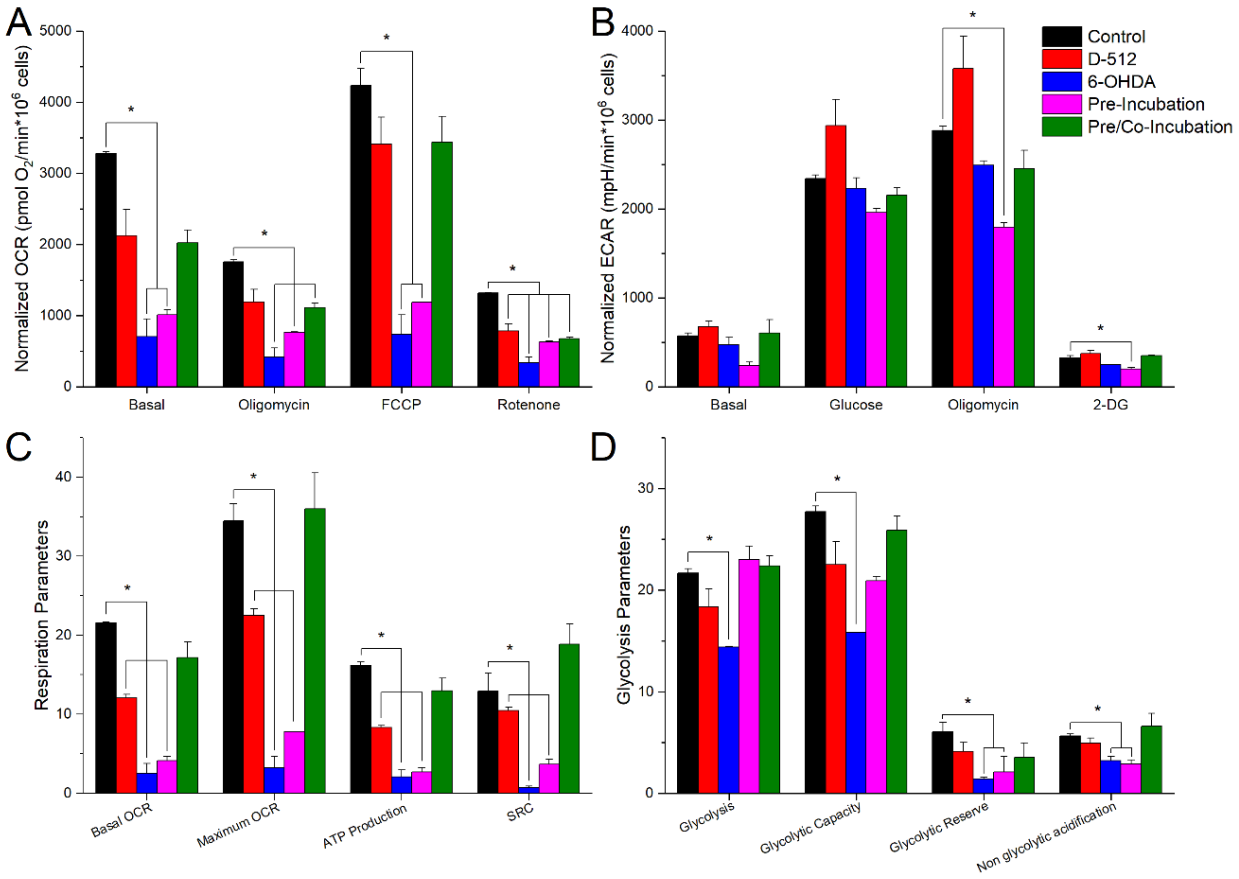

Figure 4.3: Bioenergetic outcomes and metabolic parameters - Results of the extracellular flux analysis of incubated conditions for PC12 cells. Metabolic analysis indicates deficiencies in mitochondrial parameters for cell incubated in 6-OHDA and cells incubated with a pre-treatment of D-512 followed by 6-OHDA alone. Cells incubated in D512 and those pre-treated and co-treated with D512 have no significant differences in mitochondrial parameters. *$p<0.05$, Error is +/- SEM, n=3.

Fig. 4.3b similarly shows normalized ECAR for the cell conditions. Glucose saturation yielded similar data for all cell types, with the notable exception of D-512 being increased over control. This may help explain the increased initial growth rate in fig. 4.2a. Oligomycin injection

has similar trends, excepting the large decrease in pre-incubated cells. It may be explained by damage to the mitochondria (as in fig. 4.3a) having a proportionately larger effect on the other conditions. However, this would not clearly explain why the 6-OHDA condition is not affected in the same manner.

Various respiration parameters, described in methods, is shown in fig. 4.3c. Here, differences in mitochondrial respiration between the control, D-512, and pre/co-incubation sets and the 6-OHDA and pre-incubation sets are apparent even more so. Maximal respiration, ATP production, and spare respiratory capacity all have parity between members of the first group, which are significantly greater than the calculated parameters of the 6-OHDA group.

Fig. 4.3d displays the calculated glycolytic parameters, also described in methods. Here, there is far less apparent differences in conditions than for respiration. There are only significant differences in glycolysis for the 6-OHDA against control. There is also a significant drop in glycolytic capacity for the 6-OHDA treated cells. Both cells which had 6-OHDA treatment saw significant drops in glycolytic reserve and non-glycolytic acidification.

4.3c Bioenergetically-linked Growth Indices

Fig. 4.4 compares the growth rate (fig. 4.2b) against four different bioenergetic parameters (fig. 4.3). Fig. 4.4a compares to basal respiration. A linear fit shows a strong correlation (R^2>0.95) for the conditions. Pre-incubated and 6-OHDA cells were co-localized at the lower quadrant. Pre/co-incubated and control cells were near the highest end of the trend shown here, while the D-512 cells were somewhat in between the two ends.

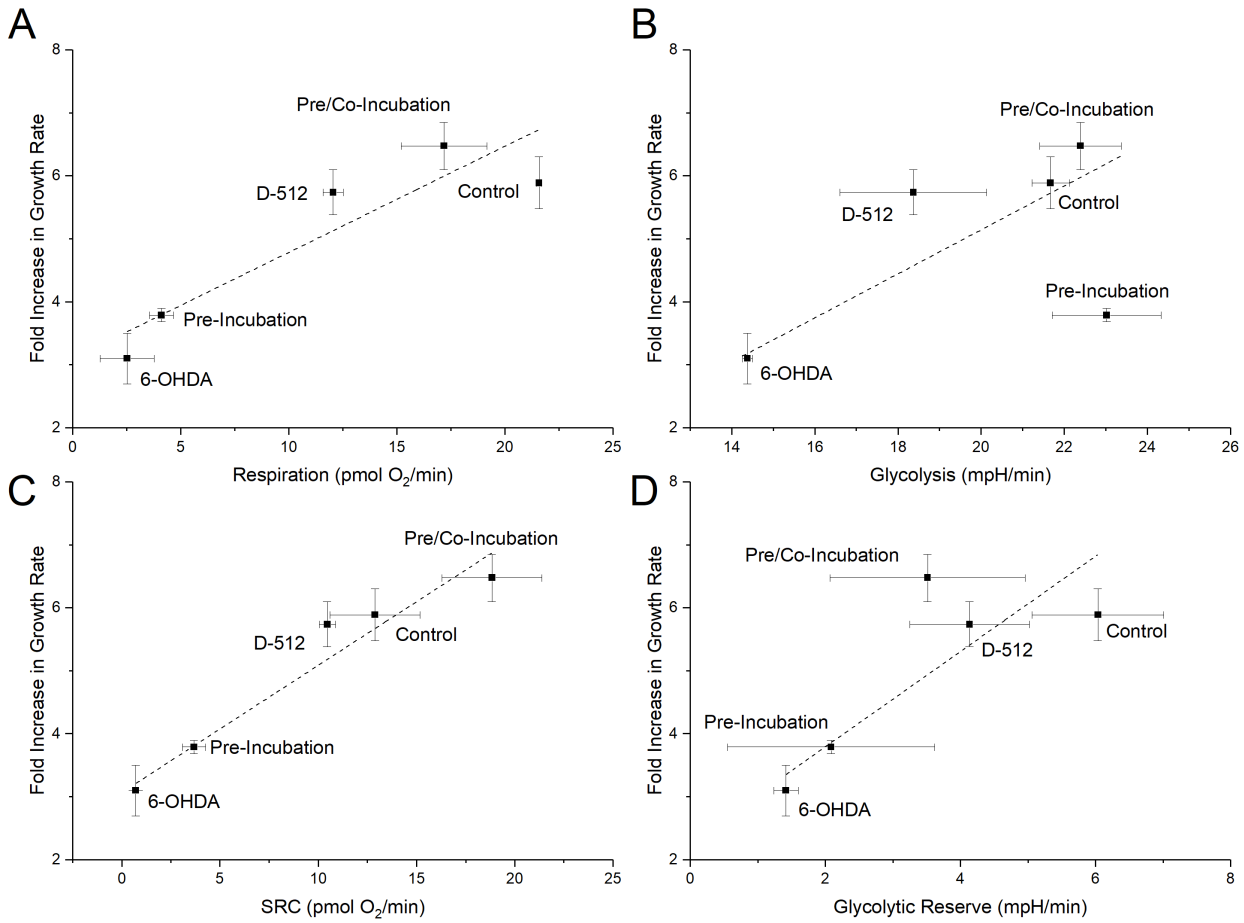

Figure 4.4: Direct comparison of bioenergetic and growth rate of various treatment groups - A) Respiration and growth rate have a very strong linear relationship across the five treatment groups. B) Spare respiratory capacity has a similar trend to A, with small variation in that control and D-512 are left shifted, indicating a lower bioenergetic efficiency. C) Glycolysis does not have any apparent trend linked to growth rate across all treatments. The line imposed is of equal slope to A to show approximate graph division. D) Glycolytic reserve has a strong linear relationship to growth rate as well. The apparent increase in slope is largely due to the low reserve levels these cells have, as in a basal state operate at high glycolytic modes. Error is +/- SEM, n=3.

Basal glycolysis, shown fig. 4.4b, had similar positions of conditions as fig. 4.4a, but had no true linear relationship. The dashed line is of equal slope to the basal respiration fitted line (fig. 4.4a), superimposed to show similar quadrant-based correlations.

Fig. 4.4c compares against spare respiratory capacity where control and D-512 conditions were co-localized, as were the 6-OHDA and pre-incubated cells. Pre/co-incubated cells were notably higher (linearly) over all other conditions. SRC has the strongest linear relationship among all parameters, relative to growth rate.

Fig. 4.4d shows the glycolytic reserve compared to growth rate. As noted in fig. 4.3d, this glycolytic parameter has similarity to the respiration parameters. Glycolytic reserve has a strong linear relationship to growth rate as well. Despite the large error ranges on glycolytic reserve, a strong linear correlation is shown. The apparent increase in slope is likely due to the low reserve levels these cells have, as in a basal state operate at high glycolytic percentages.

Fig. 4.5 compares ATP production from oxidative-phosphorylation and glycolysis pathways for all cell conditions. There is a presumption that the angle of the line intersecting the control condition and the origin can be used to infer relative disposition to respiration or glycolysis, apart from the bioenergetic modes typical of PC12 cells (α_{PC12}=71.5°). Across the spectrum of all cells, it may well be that PC12 are intrinsically offset to one metabolic pathway or another, but for the subset of only PC12, α_{PC12} should be used as the baseline. Both D-512 and pre/co-incubation conditions are slightly inclined to glycolysis compared to control. 6-OHDA and pre-incubation cell groups are extremely given to glycolysis over respiration.

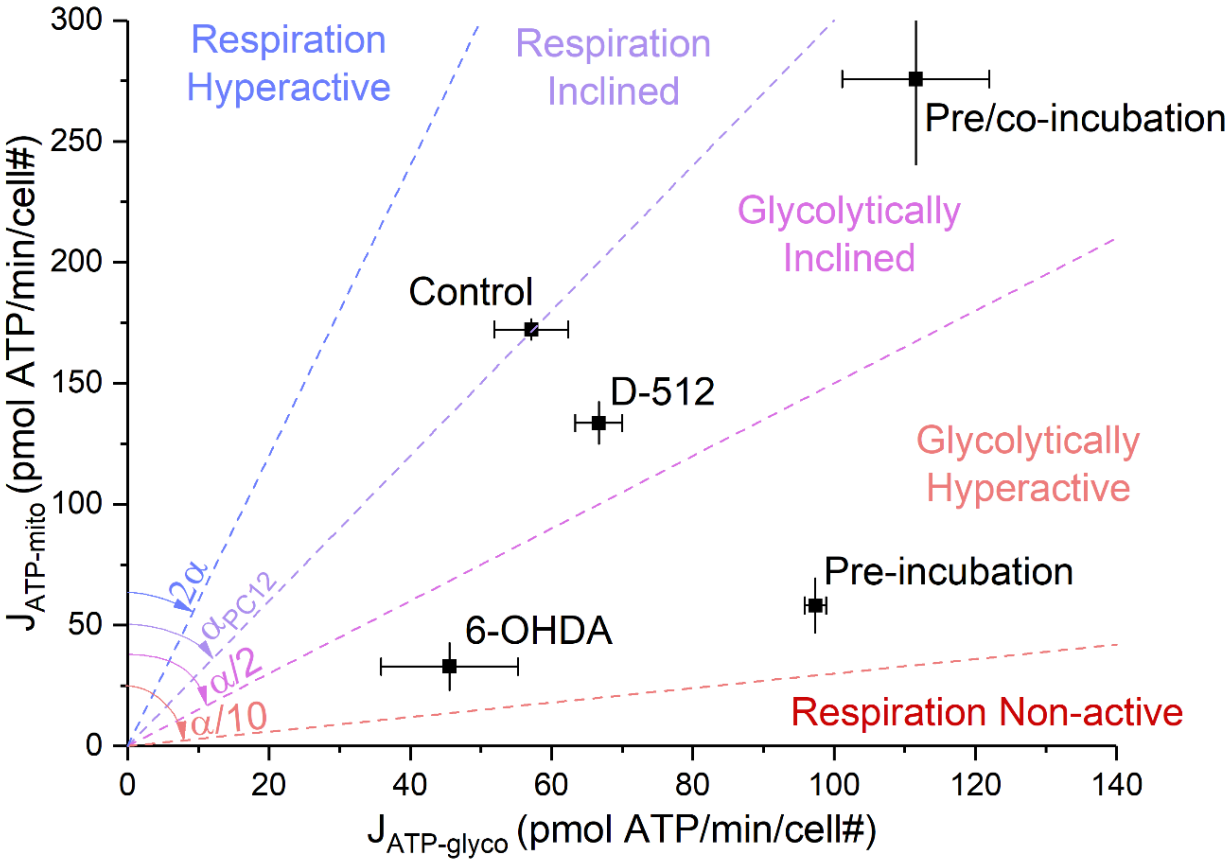

Figure 4.5: Comparison of glycolytic and respiration linked ATP production rates - ATP production values normalized to cell number were calculated from extracellular flux data, based on equations for respective glycolytic and respiration linked ATP production. Taking control as a metric for PC12 cells normal ATP production ratio, angles and extended lines corresponding to control angle (α) were superimposed to indicate related bioenergetic preferred mode.

4.3d Raman Microspectroscopy

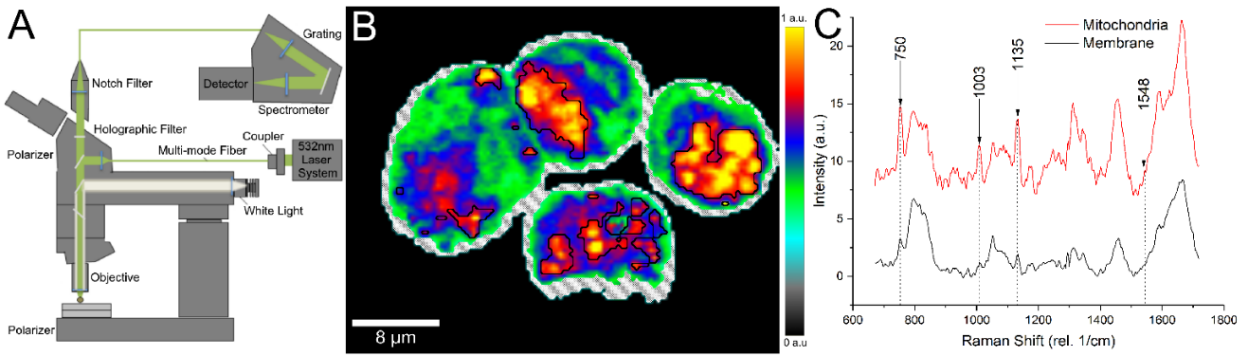

Figure 4.6: Raman microspectroscopy of PC12 cells - A) Schematic of Raman spectrometer coupled with confocal microscope and laser system. B) A Raman hyperspectral image of a group of four PC12 cells. Mitochondrial regions are marked by black outline in cells, confirmed by 750, 1135, and 1548 rel. 1/cm peaks assigned to cytochrome-c. Membrane spectra was extracted by cluster analysis and is shown as half shaded region at cells periphery. Scale shows increasing intensity with respect to maximum 750 rel. 1/cm peak. C) Spectra is total average of area contained in marked region for both mitochondria and membrane cellular regions.

The technique for acquiring hyperspectral images (fig. 4.6b) and extracted spectra (fig. 4.6c) is described in methods. Fig. 4.7a-d shows Raman hyperspectral images generated on the CH2 stretching mode (2940 rel. 1/cm) and each image is self-normalized to a scale of 0-1 a.u., with scale bar 5 um for all. Fig. 4.7a is an image of an untreated PC12 cell. Fig. 4.7b is a group of three PC12 cells which have been incubated in 10 uM D-512 for 24 hr. Fig. 4.7c shows cells which has been incubated with 75 uM 6-OHDA for 24 hr. Fig. 4.7d shows cells which were preincubated with 10 uM D-512 for 24 hr followed by coincubation with 75 uM 6-OHDA for a further 24 hr. Using the hyperspectral images in fig. 4.7a-d, fig. 4.7e displays extracted Raman spectral intensities of relevance. Spectral positions used were the phenylalanine peak at 1003 rel. 1/cm, amide I peak at 1650 rel. 1/cm and CH2 stretching peak at 2940 rel. 1/cm. There are several distinct variations in spectral ratios. Fig. 4.7f shows the spectral intensity of phenylalanine at 1003

rel. 1/cm compared to the spare respiratory capacity of respective incubation conditions. There is no difference between control and pre/co-incubated cells, whereas cells treated with 6-OHDA alone had a significantly lower ratio.

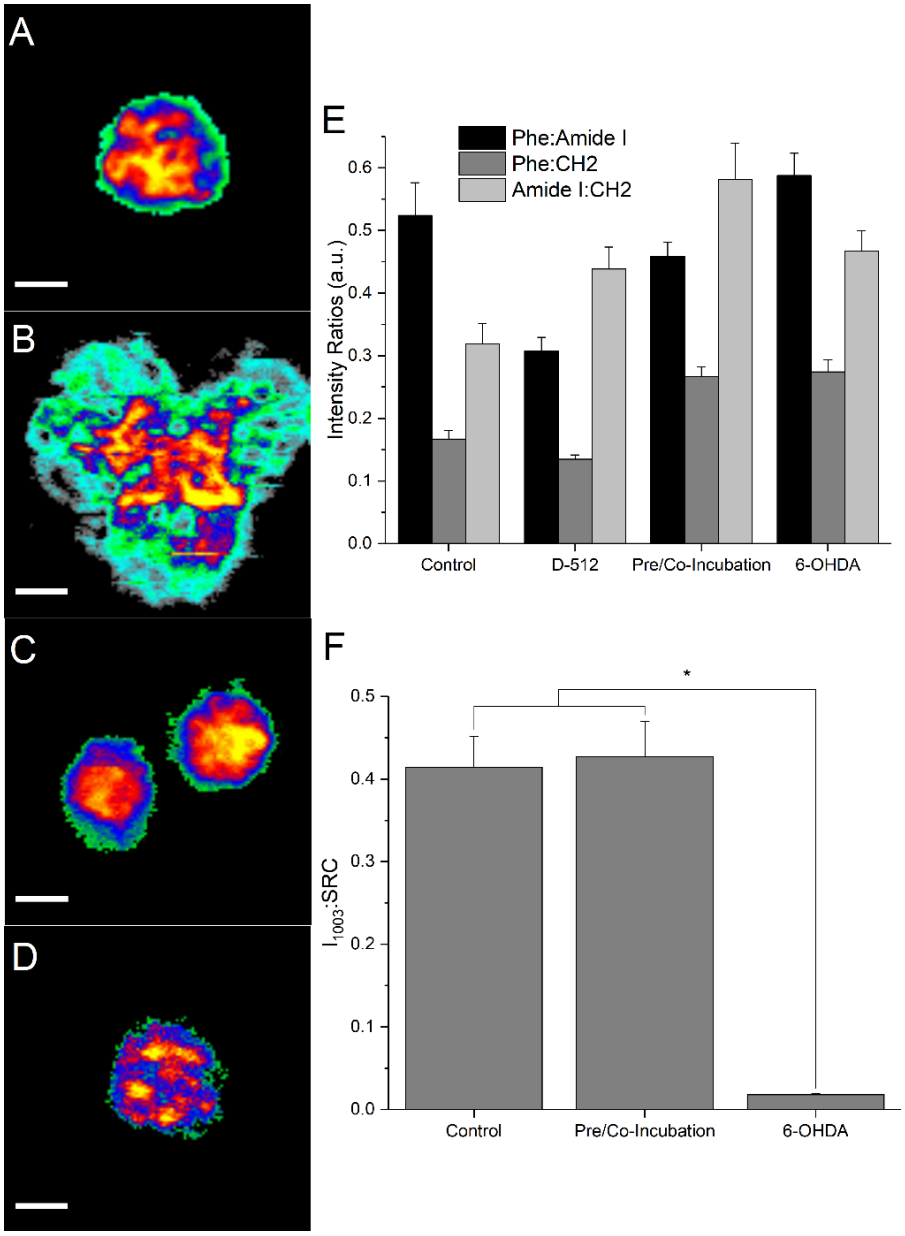

Figure 4.7: Raman hyperspectral images of various PC12 conditions - Raman hyperspectral images generated on the CH2 stretching mode (2940 rel. 1/cm) and each image is self-normalized to a scale of 0-1 a.u. A) Untreated PC12 cell. B) PC12 cells which have been incubated in 10 uM D-512 for 24 hr. This image shows three cells in a group. C) Cells which has been incubated with75 uM 6-OHDA for 24 hr. D) Cells which were preincubated with 10 uM D-512 for 24 hr followed by coincubation with 75 uM 6-OHDA for a further 24 hr. Scale bar is 5 um for all. E) Extracted Raman spectral intensities from images seen in A-D. Spectral positions used were the phenylalanine peak at 1003 rel. 1/cm, amide I peak at 1650 rel. 1/cm and CH2 stretching peak at 2940 rel. 1/cm. F) The spectral intensity of phenylalanine at 1003 rel. 1/cm compared to the spare respiratory capacity of respective incubation conditions. There is no difference between control and pre/co-incubated cells, whereas cells treated with 6-OHDA alone had a significantly lower ratio.

4.4 Discussion

Outgrowth following treatment incubation periods (Fig. 4.2A) shows minimal differences between control and D-512 conditions over the full 7-day period. The exception being a marginal increase of growth at day 3 for D-512 over control. 6-OHDA and pre-incubation conditions similarly show little difference. This would seem to indicate presence of D-512 by itself has little to no effect on overall growth. It may seem surprising that there is any growth at all, but overall cell numbers were very low compared to control, however, normalized to day 1 data, it appears growth is somewhat comparable (though still quite lower). This may be explained by certain cells having innate resistance or immunity to the neurotoxic effects of the 6-OHDA, though it was outside the scope of this study to determine that fully. The interesting feature of this graph is the pre/co-incubation condition. As shown in fig. 4.2C, the growth from day 1 to 3 is similar to that of the 6-OHDA group, about half that of control. However, from day 3 to 7, the growth is accelerated to approximately double that of control to ultimately yield an overall growth similar to control.

Bioenergetic data (Fig. 4.3) indicates similar relationships to growth among cell conditions such that control and D-512 are distinguished from 6-OHDA and pre-incubated conditions. Normalized metabolic parameters indicate that the condition which has comparable performance to control is the pre/co-incubated cells. All others groups have diminished metabolic performance to varying degrees. Differences are more apparent in ECAR data than OCR, indicating mitochondria are more strongly affected by presence of 6-OHDA, which is where is known to be inducing neurotoxic/ROS damages. This data would support that D-512 prevents such damage from agents such as 6-OHDA, which induce ROS damages in mitochondria. Such damages may increase normal metabolic response which may account for growth responses seen in fig. 4.2.

The relationship between metabolism and growth becomes more apparent when directly correlated. Strong linear correlations indicate a clear response to growth from differences in metabolism. Lower placement on the curve indicates lower overall cellular health. Deviations above the linear curve represent efficient coupling as there is higher growth per same metabolic output. Excursions below linear represent inefficiencies likely due to cellular damage and represent less growth output per metabolic unit. Some deviations may be minorly affected due to the metabolic data being immediately taken after treatment, whereas fold increase in growth is over 7 days. As such, differences in immediate and final growth may not correlate exactly. One instance of this would be the D-512 condition which would appear to have more efficient coupling than other conditions for both respiration and glycolysis comparisons. Taken for the immediate metabolism which, from fig. 4.2A, follows growth trends in that immediate growth is increased over control. Using initial metabolism as a predictor of final growth may prove useful for future trials.

Using established methods, the ATP production from both main metabolic pathways is compared for all conditions using slope analysis. Assuming control PC12 cells can be using as a reference for standard metabolic pathway ratio, other treatment conditions can be assessed. Pre/co-incubation has much higher ATP production for both pathways, over all other conditions. It is seen that the two conditions affected by 6-OHDA have severely afflicted mitochondrial function. An explanation for the elevated ATP levels for the pre/co-incubated conditions follows previous suppositions. There may be initial injury to the cells, but non-permanent, for which energy demands increase greatly to offset ROS/other damages which ultimately result in initially delayed but overall comparable to control growth.

Raman hyperspectral imaging allows for high resolution mapping of cellular features. Using known markers, mitochondrial regions are determined, and spectral signatures compared. The 1003 rel. 1/cm phenylalanine peak is resistant to environmental interference and is a high quality quantitative marker for protein content. Comparing this to the spare respiratory capacity derived from bioenergetic analysis, the aptitude of the cells to respond to OCR/ATP/energy demands per mitochondrial unit is evaluated. Supporting previous conclusions, there is no statistical difference for control and pre/co-incubated groups while the ratio for 6-OHDA is significantly diminished. Since the phenylalanine peak is insensitive to outside effects, and damage/degradation of mitochondria would increase the ratio, a decrease in ratio is largely due to a decrease in SRC. Since lower SRC represents cells operating closer to maximum levels, which has previously been posited to accord to higher energy demand and thus likely having been introduced to a destructive impetus, i.e., ROS damage. The ability to use a non-invasive spectroscopic technique to validate drug-induced differences in metabolic outcome is an invaluable research tool for drug candidate testing. It can serve to promote an analysis regime which offers; fast testing times, very low sample requirements, and broad applicability across many cell types. It is even more powerful a tool when databases of normalized cellular spectrometabolic data is logged and therefore can be used as a metric for atypical cellular function as a diagnostic tool.

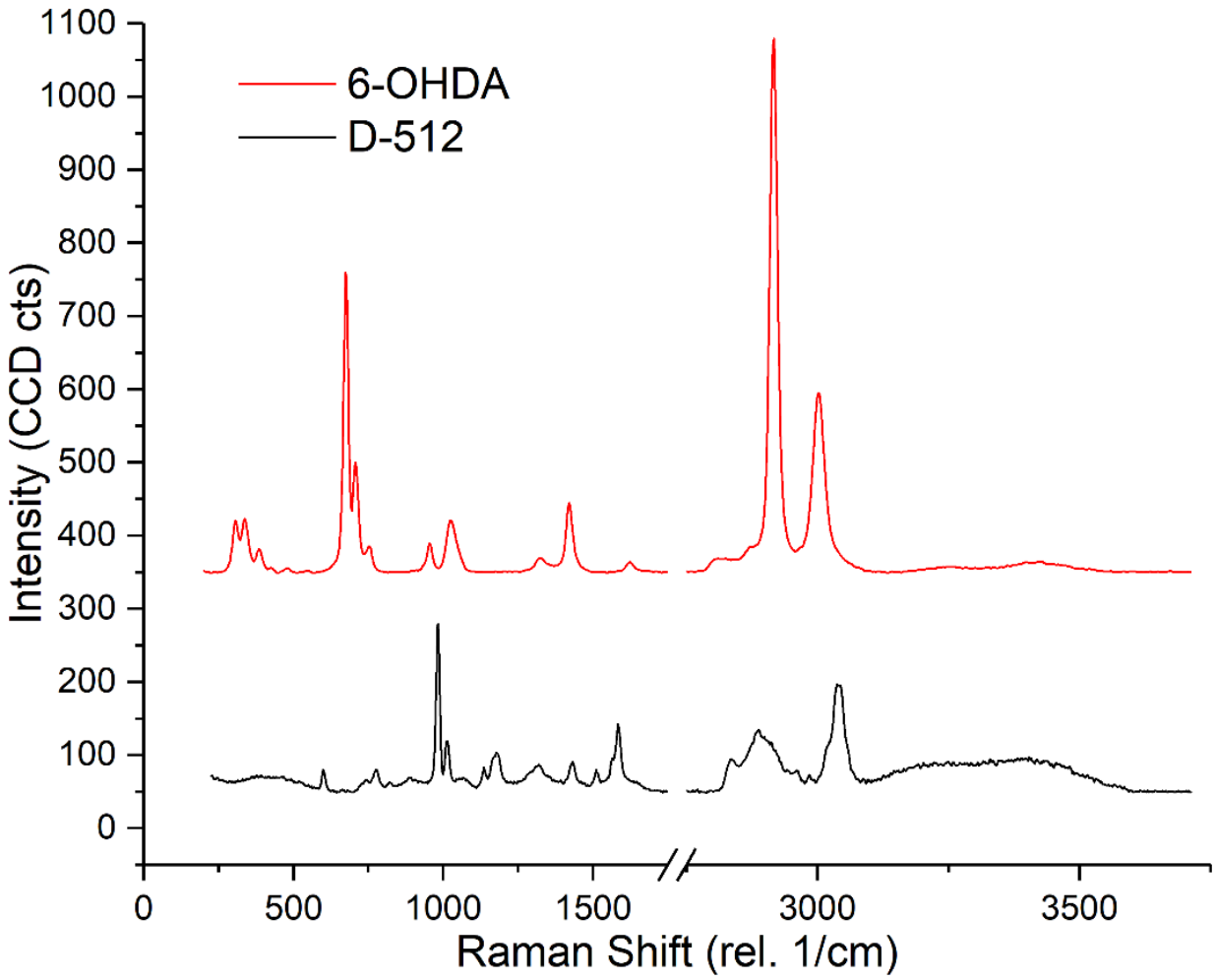

Figure 4.8: Raman spectra of pure 6-OHDA and D-512 - Pure spectra of both D-512 and 6-OHDA.

Chapter 5

Raman Microspectroscopy Indicates Membrane Stabilization as Mechanism for Cell Stabilization Conferred by the Group 3 Late Embryogenesis Abundant Protein *Afr*LEA3m

5.1 Introduction

A common molecular strategy to survive severe desiccation observed in invertebrate animals is to accumulate intrinsically disordered proteins such as late embryogenesis abundant (LEA) proteins. (Xu, 1996) Brine shrimp (*Artemia franciscana*) embryos in desiccation tolerant phases are known to expresses several different types of LEA proteins. (Sharon, 2009) Recent studies indicate that the different types of LEA proteins may play a critical role in increasing stability of different cellular targets including proteins, nucleic acids, and phospholipid bilayers. (Tolleter, 2007 & 2010) The current study aims at characterizing the protective benefits of a LEA protein derived from brine shrimp. *Afr*LEA3m is a group 3 LEA protein and expression of the protein in mammalian cells have been shown to impart significant desiccation tolerance. In this study, a combined confocal Raman microspectroscopic technique and hyperspectral image analysis technique was used to characterize the effect of ectopic expression of *Afr*LEA3m proteins in hepatocellular carcinoma cells (HepG2) under highly desiccated condition. The cells were desiccated using a fast-spin-drying technique. (Chakraborty, 2011) Detailed Raman spectroscopic analysis demonstrates that *Afr*LEA3m confers protection to cells upon acute desiccation via interaction with lipid bilayer. Upon desiccation, the intrinsically disordered proteins form into several more stable structures, with α-helix being primarily considered here. Besides offering

mechanistic protection to the lipid bilayers during acute desiccation, *Afr*LEA3m may have a distinct role to play in protecting cellular mitochondria during desiccation. This was demonstrated by bioenergetic evaluation of *Afr*LEA3m expressing HepG2 cells that were dry-processed and recovered to physiological conditions following desiccation. Viability measurements for *Afr*LEA3m cells indicate improved outcomes from dry processing compared to *Afr*LEA3m free cells.

Successful stabilization of mammalian cells is of high clinical and scientific interest. (Scott, 2005; Acker, 2005; Taylor, 2006; Fowler, 2006) Preservation in a desiccated state introduces high storage efficiencies in comparison to cryopreserved system, whereby the dry stabilized cellular system is largely independent from support systems requirements, and long-term stability at room temperature simplifies commercial transportation. (Saragusty, 2019) Several anhydrobiotic organisms have the ability to survive complete or near complete desiccation (Nakahara, 2010; Ricci, 1987), however, owing to their high sensitivity to cellular water content mammalian cells are difficult to dry process. Therefore, much focus has been given to biomimetic approaches which apply natural strategies identified in anhydrobiotic animals to mammalian systems. (Chakraborty, 2012; Hand, 2015; Chakrabortee, 2000) Previous studies demonstrated that ectopic expression of the late embryogenesis abundant (LEA) protein *Afr*LEA3m in hepatocellular carcinoma (HepG2) cells yielded 93.6% (97.7% if trehalose used in tandem) of viable cells after desiccation to ≤ 0.12g H_2O/g_{DW} employing a fast-drying technique of spin drying. (Chakraborty, 2012) While that is a big step forward in successfully dry processing mammalian cells, the challenges remain in successful long-term stabilization of cells in desiccated cells. For that reason, it is important to understand the mechanism by which *Afr*LEA3m confers protection to mammalian cells, which remains unknown. This study employs Raman microspectroscopy to elucidate how AfrLEA3m

interacts in the intracellular space which will improve understanding of the mechanism by which AfrLEA3m confers protection during desiccation.

Understanding the exact mechanism of LEA protein protection holds a special place in developing a successful strategy for dry stabilization of mammalian cells. LEA proteins belong to the larger group of intrinsically disordered proteins (Shih, 2008; Hunault, 2010) and are known to be expressed in desiccation tolerant organisms when desiccated. LEA proteins were first discovered in cotton seeds (Dure III, 1981) but have since been discovered in a variety of anhydrobiotic organisms in the phyla Arthropoda and Nematoda. In anhydrobiotic organisms, LEA proteins have been hypothesized to synergistically work with trehalose to provide protection to desiccation stresses. (Iturriaga, 2008) While the mechanism of protection offered by LEA proteins to stabilize cells and cellular components is not yet properly understood, several studies have indicated potential roles of these unique proteins in preventing protein aggregation (Boucher, 2010) and stabilization of biological membranes. It has been demonstrated that several LEA proteins assume additional secondary structures, such as α helices, β sheets, and hairpin loops during desiccation. (LeBlanc, 2019; Shimizu, 2010)

In the current study a group 3 LEA protein derived from *Artemia franciscana*, *Afr*LEA3m was used to characterize the nature of desiccation tolerance offered by LEA proteins. *Afr*LEA3m protein has been shown to confer water-stress tolerance in HepG2 cells and is known to be synthesized in the cytoplasm and accumulate in the mitochondrial matrix. (Boswell, 2014 & 2014) While it is understandable that expression of *Afr*LEA3m in a mammalian cell may improve mitochondrial stability, it was also observed that cells expressing *Afr*LEA3m also had higher membrane integrity following rehydration. In this study confocal Raman microspectroscopy and hyperspectral imaging techniques to characterize the effect of intracellular expression of

*Afr*LEA3m in HepG2 cells in both desiccated and hydrated conditions. Cells were dried uniformly to a highly desiccated state (0.2 g_{H20}/g_{DW}) in an inert environment using the fast-drying technique of spin drying to limit time duration for osmotic excursions. Trehalose was used in the desiccation medium to offer lyoprotection during drying. The confocal Raman microspectroscopy technique used here has the advantage of specially determining chemical characteristics in both the intracellular and extracellular space. Special attention was given to mitochondria and cellular membrane analysis as key indicators of overall health and metabolism. Cell membrane is an important injury site while lyoprocessing mammalian cells and this technique was used to compare the chemical characteristics of the cellular membranes expressing *Afr*LEA3m and control cells in both hydrated and desiccated conditions. Change in membrane characteristics were also evaluated before lyoprocessing and following rehydration. Effect of expression of *Afr*LEA3m on cellular metabolism was also evaluated and compared pre-and post lyoprocessing using spin drying. The current study indicates the possibility of group 3 LEA proteins such as *Afr*LEA3m having a protective effect both on cell membrane and mitochondrial function and both of these protective effects may originate from its ability to protect the mitochondrial membrane during desiccation.

5.2 Materials and Methods

5.2a Cell Culture

Human hepatocellular carcinoma (HepG2) cells were stably transfected using a tetracycline (Tet)-inducible expression system to express the *Afr*LEA3m protein, as previously described. (Chakraborty, 2012) Briefly, a Tet-inducible gene expression system in HepG2 cells

was developed by stable transfection with a gene encoding the Tet-transactivator protein. The original nucleic acid sequences for *Afr*LEA3m were cloned from *A. franciscana* embryos and was optimized for human codon bias. The codon optimized nucleic acid construct was next inserted into a Tet-On expression vector (pTRE3G) and stably transfected into HepG2 Tet-On cells and stable clones were obtained after selection with G418 at 800 µg/mL for 6 weeks. Clones were selected for high induction of *Afr*LEA3m by tetracycline and cultured without induction in Opti-MEM (Gibco, Carlsbad, CA) supplemented with 5% fetal bovine serum (Gibco) and penicillin-streptomycin (100 units/mL penicillin G, 100µg/mL streptomycin sulfate; HyClone-Thermo Scientific, Logan, UT) under standard cell culture conditions (95% air, 5% CO_2, and 37°C). Cells were grown in 75 cm^2 cell culture flasks (Corning Incorporated, Corning, NY) and allowed to reach a maximum confluency of 90%. Cells were dislodged with 0.05% trypsin centrifuged, and counted with a hemocytometer (Hausser Scientific, Horsham, PA) and 0.04% Trypan Blue exclusion stain (ThermoFisher, Waltham, MA) to enumerate live cells.

5.2b Acute Desiccation Using Spin Drying

Cells were plated on collagen coated quartz windows (20 mm Ø, Edmund Optics, Barrington, NJ) at a density of $5x10^4$ cells per disc. After 24 h incubation with 0.5 µM doxycycline to induce *Afr*LEA3m expression, the cells on the quartz windows were spin-dried using a Cee 200X (Brewer Science, Rolla, MO) as described prior (Chakraborty, 2012) Briefly, 250 µL of a 37°C trehalose-based desiccation solution (1.2 M trehalose, 10 mM KCl, 5 mM glucose, 20 mM HEPES, 0.5 mM K_2HPO_4, 0.5 mM KH_2PO_4, 20 mM glycerol, and 120 mM betaine; pH 7.4) was pipetted to cellular surface after washing with PBS. The spinning regime was set to 1000 RPM

for 55 s, followed by a ramp to 3000 RPM for 5 s. This was done under an environment of dry nitrogen gas.

5.2c Raman Microspectroscopy

Raman microspectroscopic measurements were carried out with a customized confocal microscope and Raman spectrometer combination (UHTS 300, WITec Instruments Corp., Germany). Raman spectra were collected using an EMCCD camera (Andor Technology, UK). A 532 nm solid state laser calibrated to 20 mW was used for excitation and spectra were collected using a custom 50X high resolution objective (Mitutoyo, Japan). Area spectral arrays were collected at 250 nm intervals, with an integration time of 0.5 s. Raman hyperspectral images were collected for six conditions in total. Unprocessed cells for both unexpressed and *Afr*LEA3m expressed cells were taken as normal physiological conditions. Spin dried cells were unexpressed and *Afr*LEA3m expressed cells in the desiccated state. Rehydrated unexpressed and *Afr*LEA3m expressed cells are those which were dry processed (spin-dried) and then immediately recovered to standard media conditions. The hyperspectral images were generated by integrating the CH2 stretching region, and then individually normalized to the integrating peak, so that all images used a color scale of 0 to 1 a.u. Raman spectra obtained from area array scans and processed to subtract background and substrate spectra using WITec Project 4 software. Further deconvolution analysis was conducted with Peakfit v4 software based on a 2nd derivative fitting algorithm (Systat Software, Inc., San Jose, CA), and Origin Pro 2018 (OriginLab, Northampton, MA). The higher wavenumber region from ~2700-3700 rel. 1/cm contains both CH2 stretching and OH stretching vibrational modes. The following assignments in deconvolution analysis were made; CH2 symmetric (2880 rel. 1/cm), CH2 asymmetric (2940 rel. 1/cm), OH low (3060 rel. 1/cm), OH

symmetric (3220 rel. 1/cm), OH asymmetric (3420 rel. 1/cm), and OH high (3590 rel. 1/cm). These last four represent OH stretching modes in descending order of H-bonding strength. A representative Raman spectrum of a control HepG2 cell in imaging solution, plotted with a 6-component deconvolution, is shown in Fig. 5.9.

5.2d Desiccation via Sessile Droplet

Pure 42.5 mg/mL *AfrLEA3* protein was dried in a 5 µL sessile droplet and monitored for moisture change. This was done by both gravimetry (Mettler Toledo XP26, Columbus, OH) and by Raman spectroscopy. The droplet was deposited on a slide and intermittent weights were taken and recorded with respect to time. After five measurements of no change, it was assumed to be maximally dried with respect to room conditions. The same droplet was deposited on a quartz slide for Raman acquisition. The I_{3400}:I_{2920} spectral ratio is representative of the total water amount (OH-stretching band) with respect to the protein concentration (CH2-stretching band). Spectral were collected after minor calibrations to account for shifting droplet dimensions. Acquisition was concluded when steady spectra response was observed.

Both HepG2 and transfected cells were grown, collected, and suspended with PBS in cryotubes to a concentration of $1x10^7$ cells/mL. These were put through a freeze-thaw cycle five times (liquid nitrogen into 37°C water bath) to lyse the cells. Lysates were pushed through 0.22 µm syringe filters (Target2 PES, ThermoFisher) to remove cellular particulate. Lysate of both cell types were then scanned with Raman to determine sensitivity in determining characteristic differences between *Afr*LEA3m expressing cells and normal HepG2 cells, with a focus on comparing to non-invasive single cell intracellular scans.

A mitochondria extraction was performed on HepG2 cells using a microcentrifuge-based kit (Mitochondria Isolation Kit for Cultured Cells, ThermoFisher, Waltham, MA). Briefly, 2x10^7 cells were treated with kit reagents, homogenized, and then processed with several centrifugation steps between 700 x g and 12000 x g at 4°C. The isolated mitochondria extract was used in the same manner as the cell lysates, both for drying and Raman acquisitions.

These samples were mixed with pure 42.5 mg/mL *AfrLEA3m* protein at a 1:1 ratio. These were deposited on gold slides to be dried until in equilibrium with the environment, as shown in figure 5.11. Raman acquisition of the sessile droplets were taken before and after drying. The spectra were compared by taking the ratio of the 1320 rel. 1/cm peak, representing amide III secondary structure here α-helical groups and the 2920 rel. 1/cm peak, representing the CH2 stretching band. This indicates the relative amount of secondary structure with respect to the concentration of overall protein, on a spectroscopic basis.

5.2e Bioenergetic Evaluation

Analysis of metabolic function were carried out on an extracellular flux analyzer (XFp Seahorse, Agilent Technologies, Santa Clara, CA). Cells were seeded in microwell plates at a seeding density of $2x10^4$ cells per well. Both oxygen consumption rate (OCR) (representing mitochondrial respiration) and extracellular acidification rate (ECAR) (representing glycolysis) measurements were obtained. Briefly, XFp cartridge sensors were hydrated and injection ports were loaded with oligomycin (1 μM), carbonyl-cyanide-4-(trifluoromethoxy) phenylhydrazone (FCCP, 0.5 μM), and rotenone/antimycin A (0.5 μM). Reagents used for glycolysis testing were D-glucose (10 mM), oligomycin (1 μM), and 2-deoxyglucose (2-DG, 50 mM). Oligomycin was used to inhibit F_0F_1-ATPase to get an approximate measurement of proton leak respiration. FCCP

acts as an uncoupling agent that collapses the mitochondrial proton gradient and thereby uncouples oxidation from phosphorylation, maximizing oxygen consumption rates. The contribution to OCR via non-mitochondrial processes was quantified using rotenone and antimycin A, which inhibit complex I and III of the respiratory system, respectively. Glucose was supplied as to fully saturate basal ECAR. Oligomycin is injected to inhibit ATP synthase, arresting ATP production via oxidative phosphorylation, which then induces the cells to respond by increasing glycolysis to maximum levels, resulting in higher ECAR. 2-DG is a glucose analog which competitively inhibits hexokinase, effectively stopping glycolysis.

5.3 Results

The protein fingerprint region in Raman spectroscopy, containing significant amide peaks located at approximately 1200-1800 rel. 1/cm, yields the majority of cellular information and so is given particular attention. In Fig. 5.1A, the amide I group is shown located at ~1650 rel. 1/cm. Amide II is located at ~1450 rel. 1/cm while Amide III is located at ~1320 rel. 1/cm. Raman spectroscopy presents the ability to view hyperspectral information with spatial definition. This is employed in Fig. 5.1B1-B4 to distinguish three cellular compartments of interest: total average cell, mitochondria, and membrane, with a corresponding merged image. Each of these has an average spectrum associated with it, shown in Fig. 5.1C.

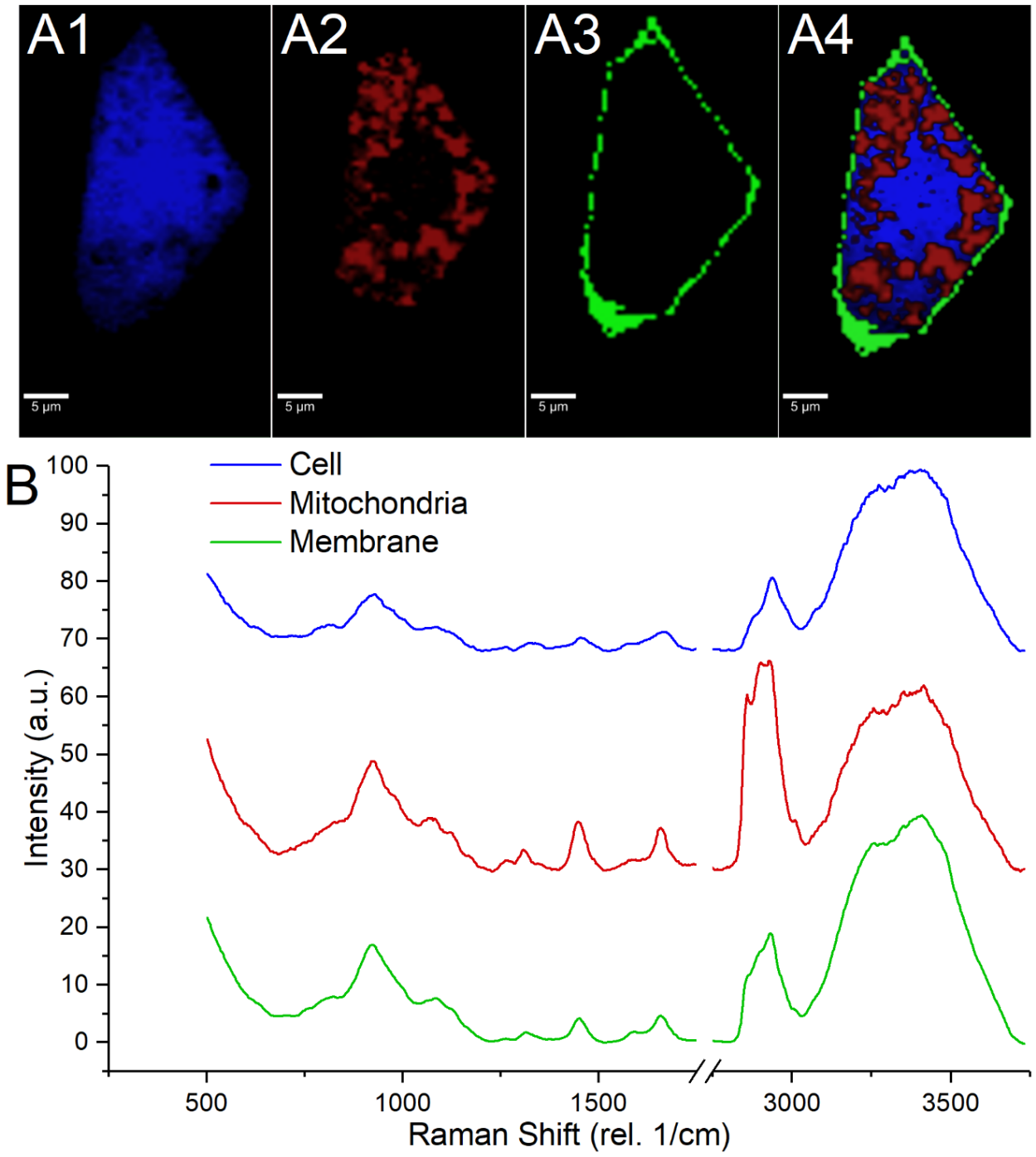

Figure 5.1: Representative Raman spectra of a hepatocellular carcinoma cell - A1) Hyperspectral Raman image of live hepatocellular carcinoma cell in culture conditions. The images were created using component analysis and by integrating spectral signatures collected from intracellular space. Figures A2 and A3 indicate distribution of mitochondrial and cellular membrane. Fig. A4 represent the composite image created by merging spectral signatures from A1-3. The color mapped spectra are derived from intracellular regions and used for component analysis are shown in (B).

HepG2 *Afr*LEA3m expressing cells were compared with non-expressing cells and the spectra for both were normalized against their respective CH_2 symmetric peaks for protein evaluation, shown in Fig.5. 2A. Fig. 5.2B is the normalized amide peak values for both cell conditions, showing slightly increased relative protein amount in the *Afr*LEA3m expressed cells. Both HepG2 *Afr*LEA3m expressing cells and non-expressing cells were lysed as previously described and evaluated in the same manner as single cell scans (Fig. 5.2C). Normalized protein content shows similarity between cells groups for both sample types.

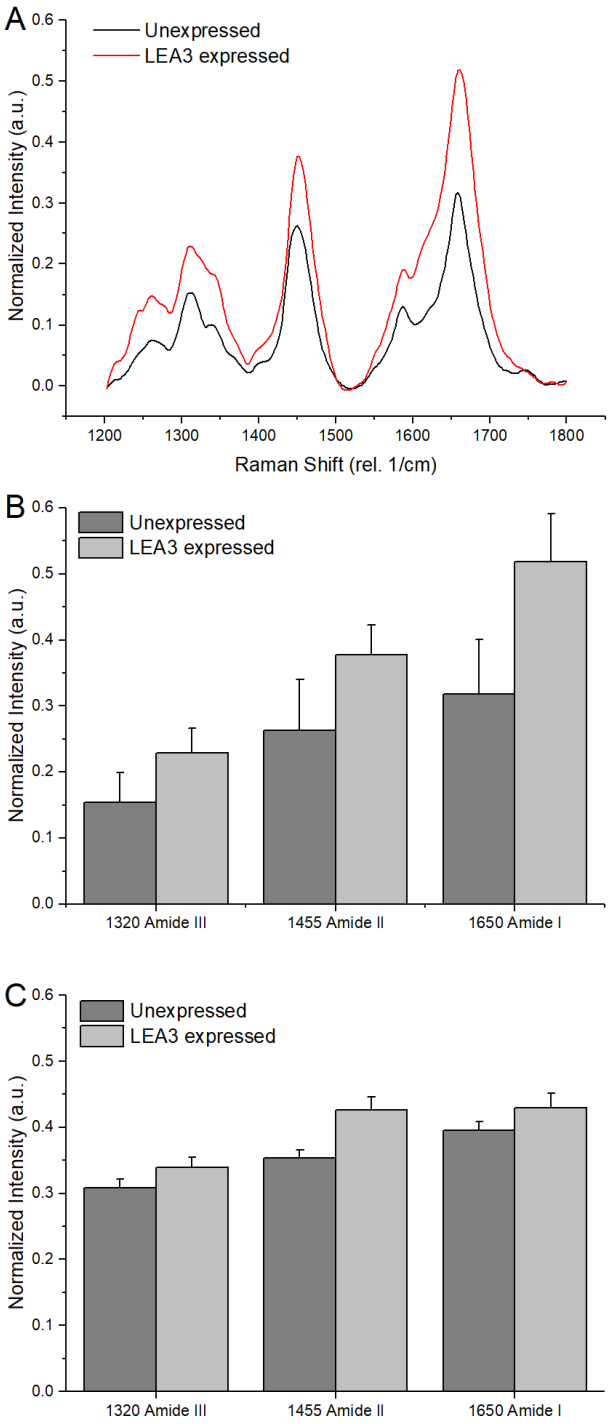

Figure 5.2: Comparison of unexpressed and *Afr*LEA3m expressed HepG2 cells - A) Amide peaks contained in fingerprint region shown in cells expressing AfrLEA3m compared to control cells. for both cell conditions, normalized to the CH2-stretching peak (2940 rel. 1/cm). B) Enumeration of (A) showing higher relative concentration of protein in AfrLEA3m expressed cells. C) Cell lysate from both cell types was collected and scanned as a bulk solution. There is a very high degree of agreement between physiological intracellular spectra and cell lysate spectra.

Figure 5.3 displays time dependent drying of sessile droplets containing pure *Afr*LEA3*m* protein at a concentration of 42.5 mg/mL. Fig. 5.3A graph shows that the droplet has approximately 90% of water removed via evaporation over the course of 17 minutes. Fig. 5.3B similarly displays the loss of water via evaporation, but on a spectral basis. Here, there is an approximate 95.5% reduction is intensity ratio of the I_{3400}:I_{2920} peaks. The two methods combined provides for a means to compare the spectral ratio to standard residual moisture content on a mass basis. The gravimetric apparatus is more tightly enclosed against the ambient than the Raman microscope stage, which likely explains why it takes longer to reach a steady dryness level.

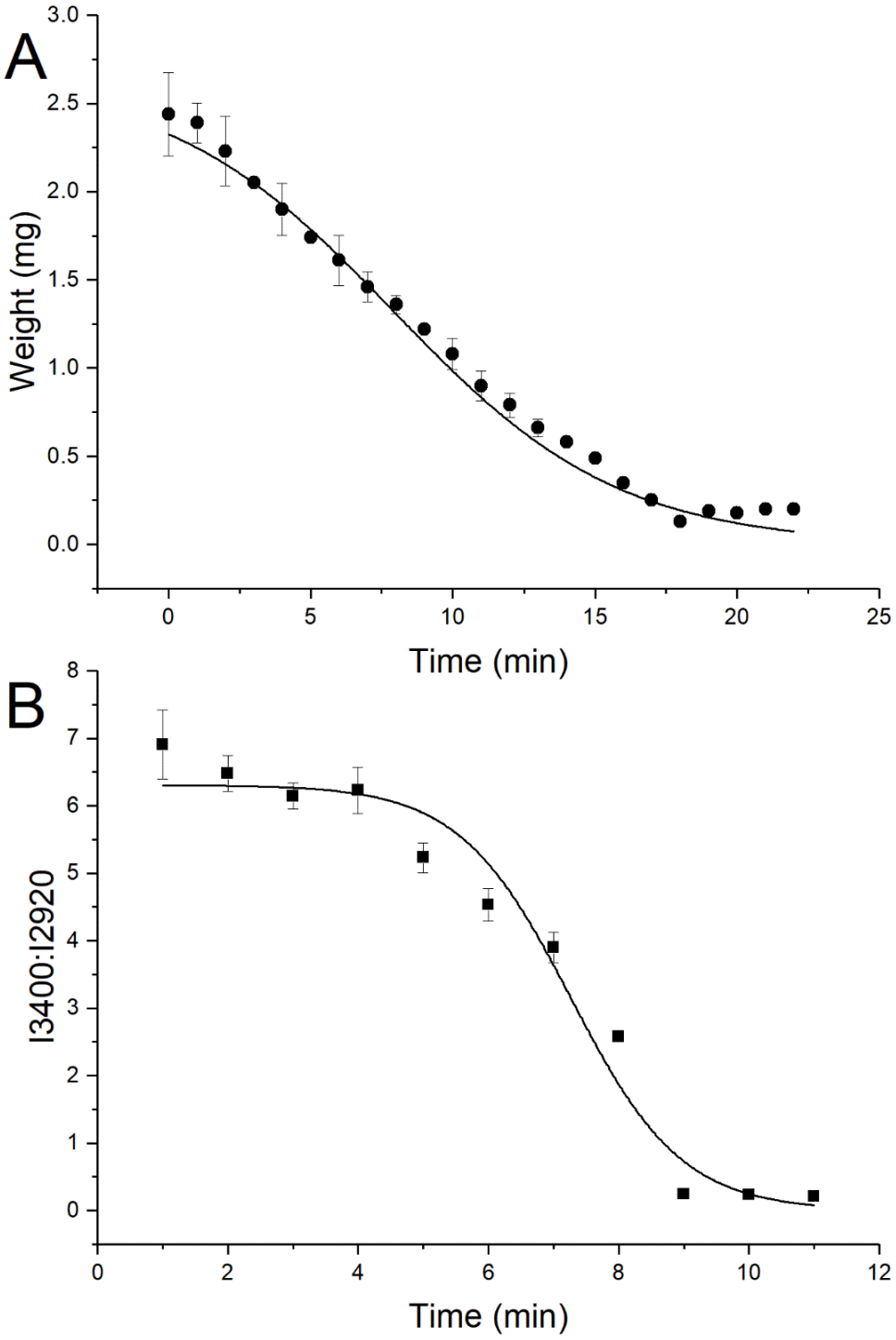

Figure 5.3: Drying of pure *Afr*LEA3m protein - A) Weight obtained via gravimetry of a droplet of 42.5 mg/mL purified *AfrLEA3* protein. B) The I_{3400}:I_{2920} spectral ratio signifies the water content relative to the amount of protein in the analyte. The same volume of droplet as used in gravimetric analysis was used for the spectral technique as well. A similar trend is shown for water content for both spectral and gravimetric techniques. Both plots have overlaid sigmoidal fits. Error bars show SEM, n=3.

HepG2 cell lysate and isolated mitochondria suspension was collected as described in methods. Fig. 5.4A displays the spectral change in relative α-helical structure of cell lysate with and without being mixed pure *Afr*LEA3*m* protein. There was a decrease in I_{1320}:I_{2920} ratio for the cell lysate upon drying, explained mostly by the artifact of the 2920 rel. 1/cm peak increasing concentration with drying. The I_{1320}:I_{2920} ratio increases when the lysate is spiked with the pure protein. For the isolated mitochondria (Fig. 5.4B), there is a small increase in I_{1320}:I_{2920} ratio upon drying. There is a much stronger increase for the mitochondria lysate when protein solution was included. Figure 5.4C represents the change in drying performance upon addition of pure protein solution between the cell lysate and the isolated mitochondria, on an absolute basis. The distinguishing difference between the sample groups would be the difference in total lysate against the mitochondria extraction. This is supported by that both solutions with *Afr*LEA3*m* protein inclusion upon drying reach the same approximate I_{1320}:I_{2920} ratio of 0.4 a.u.

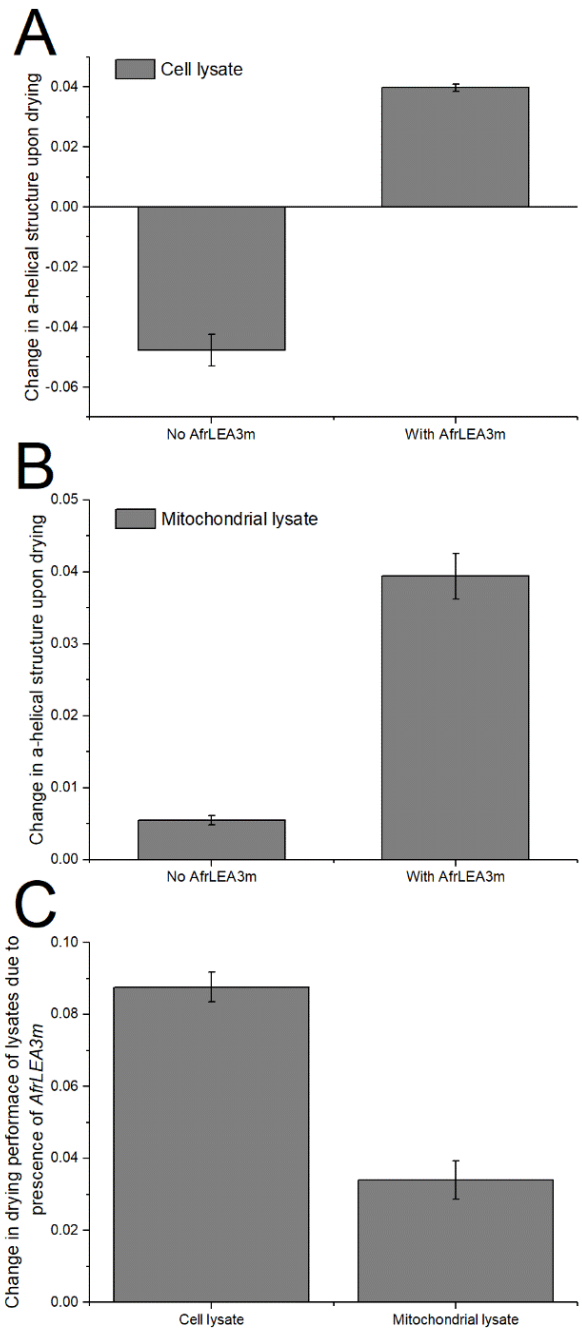

Figure 5.4: Impact of *AfrLEA3*m upon desiccation characteristics of droplet dried cell and mitochondrial lysates - A) Comparison of the difference ratio for amide III group with spectral center at 1320 rel. 1/cm, indicating secondary structure, here α-helical groups, and the 2920 rel. 1/cm CH2 stretching band from aqueous to desiccated form. This ratio is shown for both pure cell lysate and lysate which has been mixed with pure *AfrLEA3m* protein. B) The same ratio as in (A) was taken but for isolated mitochondrial that was processed into lysate. For both cellular lysate and mitochondrial lysate, an increase in ratio was much greater upon drying when containing *AfrLEA3m.* C) The relative difference between the impact *AfrLEA3m* has upon both cell lysate and mitochondrial lysate, the difference in ratios shown in (A) and (B).

Hyperspectral maps were generated for unexpressed and *Afr*LEA3*m* expressed cells in the desiccated state (Fig. 5.5). The 755 rel. 1/cm peak corresponding to cytochrome c and 1308 rel. 1/cm peak corresponding to α-helix protein structure were used for integration and intensity mapping. For each cell type, a representative single cell scan was used to show co-localization between molecules of interest. A white dotted outline shows the actual cell membrane as viewed by polarized light microscopy. The results show highly correlated α-helix (Fig. 5.5A, B) and cytochrome c (Fig. 5.5C, D) regions. The intensity for both cytochrome c and α-helix regions are much higher for *Afr*LEA3*m* expressing cells (Fig. 5.5B, D) compared to unexpressed cells (Fig. 5.5A,C).

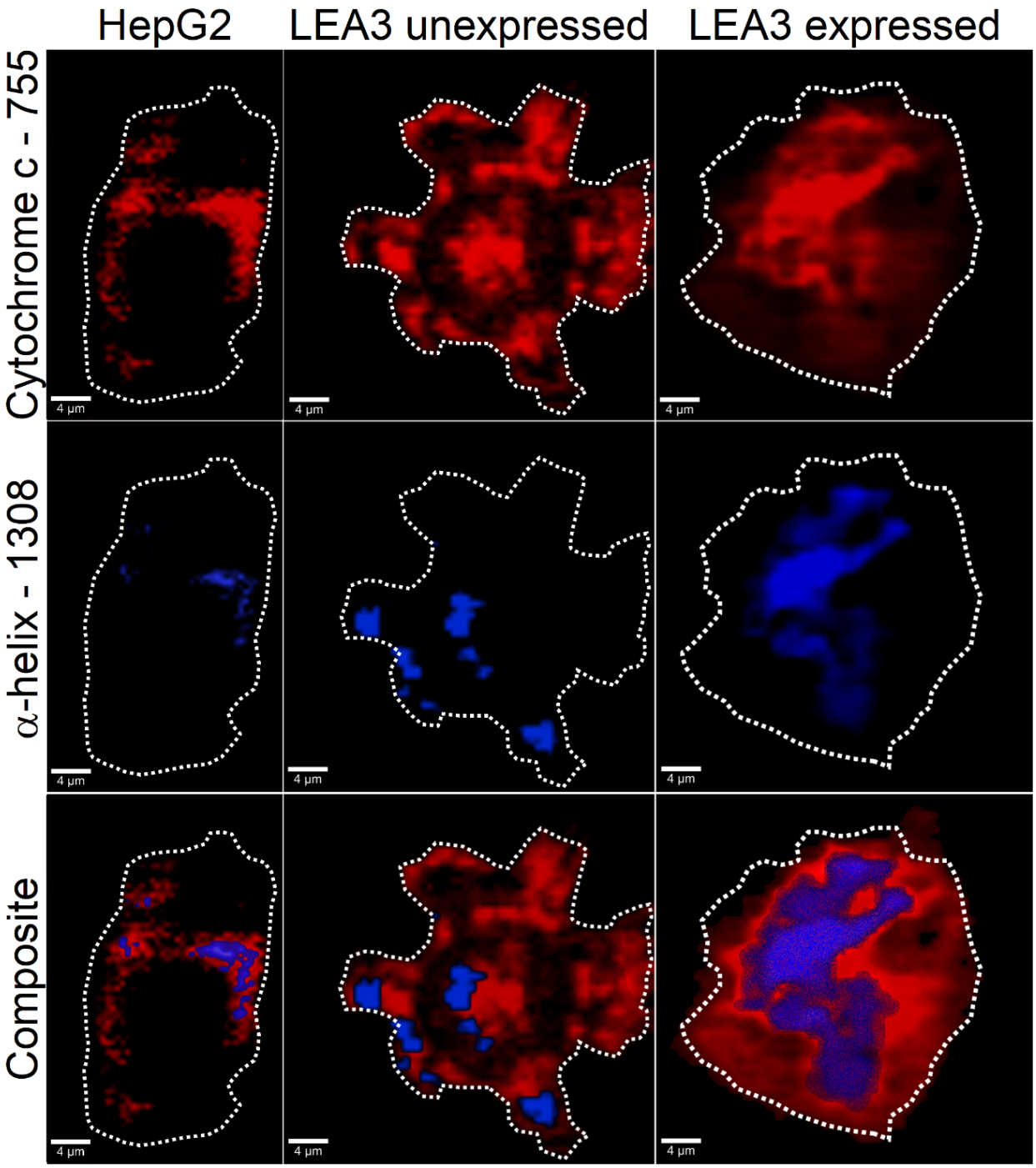

Figure 5.5: Hyperspectral image correlation of α-helix structure in desiccated environment - Raman hyperspectral images were integrated on the 755 rel.1/cm cytochrome c peak (red) and the 1308 rel. 1/cm α-helical peak (blue), with composite merge shown. The images shown were acquired in desiccated state for control (HepG2), and stably transfected AfrLEA3 HepG2 cells with and without doxycycline inducement. There is much higher degree of α-helical structure directly correlated to cytochrome c signature in AfrLEA3 expressed cells over others. Outlines of actual cell membranes are shown as dotted lines.

Subcellular components were evaluated employing Raman spectroscopy. The cellular membrane was given attention due to strong relation to desiccation injury. (Solocinski, 2018) Figs. 5.5A and 5.5B show the cellular membrane mask generated by hierarchal cluster analysis which accords to the cells shown in Fig. 5.5 rehydrated cells for unexpressed and *Afr*LEA3m expressed conditions, respectively. Fig. 5.5C shows the protein evaluation for the membrane. The is no difference between amide I and III spectral regions. However, there is an increased normalized amide II intensity for unexpressed cells compared with *Afr*LEA3m expressed cells. Fig. 5.5D takes consideration of the mitochondrial regions, by considering cytochrome c peak (1127 rel. 1/cm) in the Raman hyperspectral arrays. This was taken as a ratio to the mitochondrial poise from the bioenergetic data to yield a spectrometabolic appraisal between the two cell conditions. There is a significant difference, with the cytochrome c/mitochondrial poise ratio being higher for *Afr*LEA3m expressed cells.

From the hyperspectral maps in Fig. 5.3, averaged spectra were extracted and compared. Fig. 5.4A shows these spectra with the two previous peaks of interest annotated, for the 755 rel. 1/cm and the 1308 rel. 1/cm. The increased cytochrome c peak indicates increased mitochondria for the cell. Fig. 5.4B displays the normalized α-helix intensity to total organic content. The α-helix peak intensity is only present in the AfrLEA3 expressed cells. This is evidence for the increase in AfrLEA3 conformational shift from disordered to α-helix structure upon entering the desiccated state.

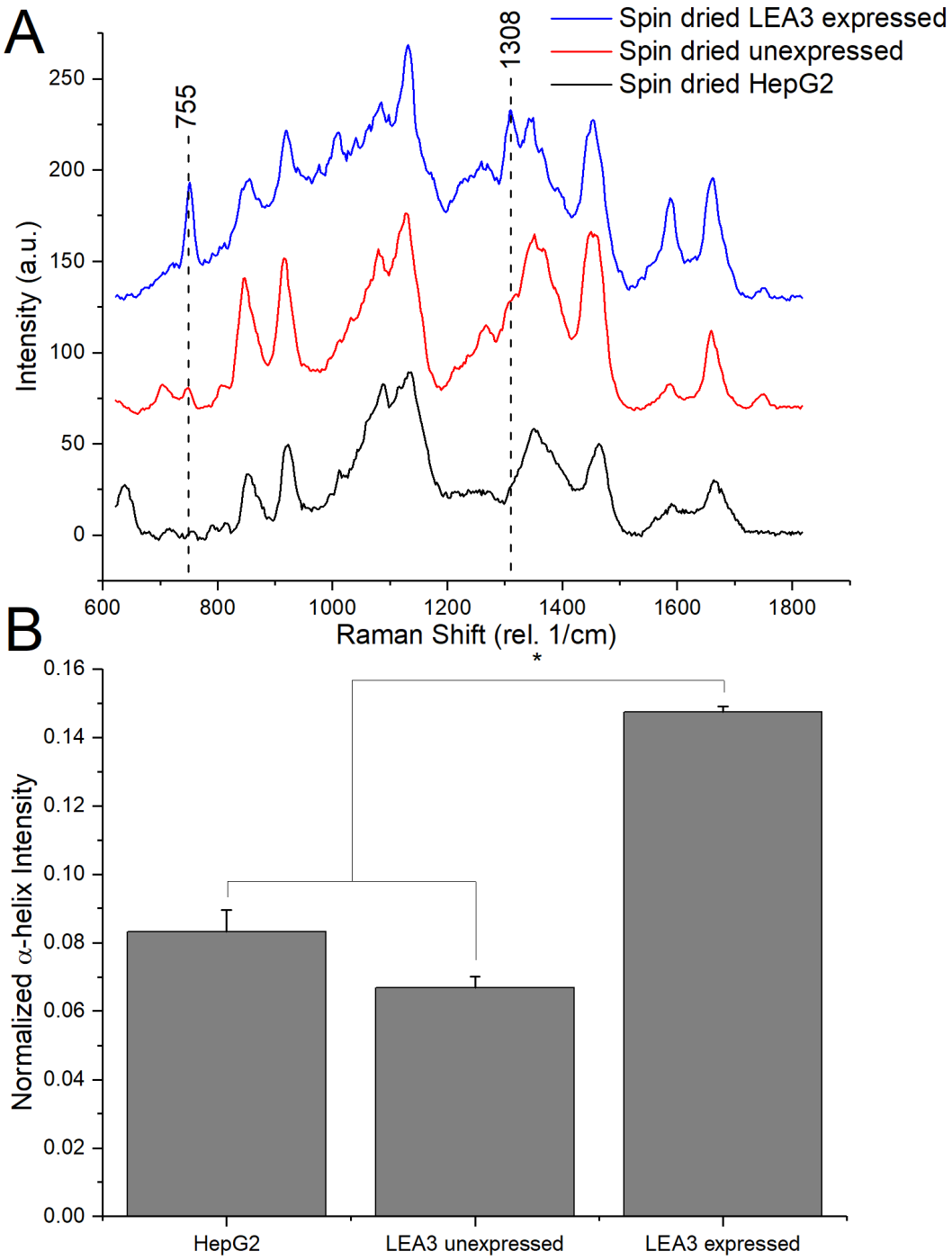

Figure 5.6: Raman evaluation of α-helix structure for *Afr*LEA3m - A) Averaged spectra acquired from hyperspectral images of the three cell conditions. There are several notable differences in spectra, notably the α-helix peak at 1308 rel. 1/cm. B) Intensity of 1308 rel. 1/cm peak normalized to 2940 rel. 1/cm CH2 stretching peaks. AfrLEA3 expressing cells display a significantly higher degree of secondary protein conformation when induced via drying compared to control and unexpressed cells.

For the non-transfected cells, *Afr*LEA3m cells showed higher overall protein intensity than unexpressed cells. This was independent of hydration level and also observed in the spin-dried cells. This was not the case with rehydrated cells where there were rather significantly decreased protein levels in *Afr*LEA3m cells. The dramatic shift in normalized protein concentrations in the spin-dried cells was expected; amide I contributions all but disappear as they are strongly related to water interactions. The increased amide III intensity of the *Afr*LEA3m cells over unexpressed are also expected as the *Afr*LEA3m proteins becomes more structured (α-helix, β-sheet) upon acute desiccation.

Fig. 5.7 displays bioenergetic data acquired from extracellular flux analysis and derived metabolic parameters. Control and *Afr*LEA3m cells were compared before and after spin drying 3 days after rehydration. No difference for basal respiration among unprocessed cells and non-transfected spin-dried cells was observed. There was a significantly higher basal rate for spin dried *Afr*LEA3m cells. Upon oligomycin injection, cells had a predictable drop in OCR, by about 27.1%. FCCP increased OCR to maximum, to 122.1% of basal. Acute rotenone and antimycin A injection dropped OCR levels to 44% of basal.

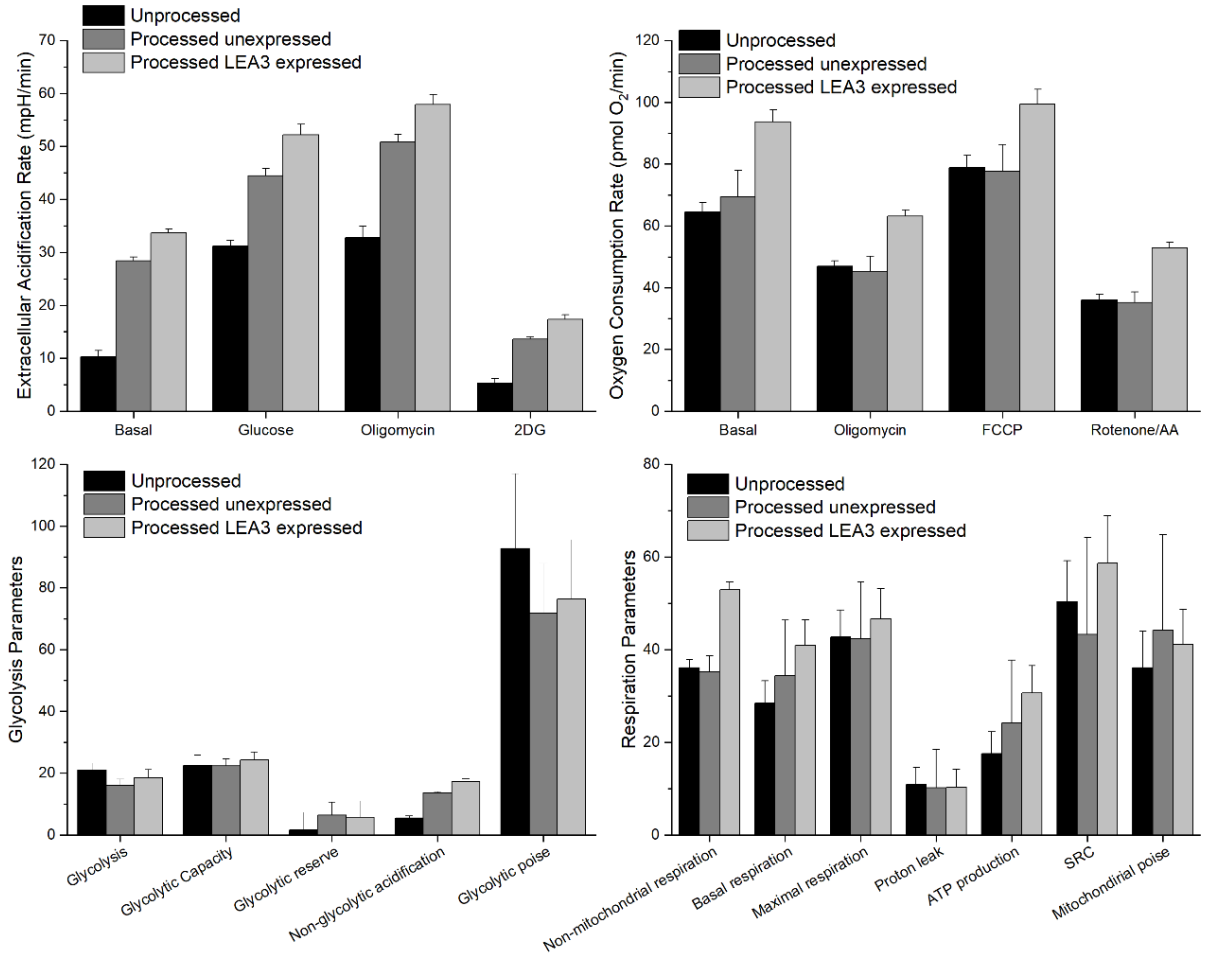

Figure 5.7: Bioenergetic outcomes and metabolic parameters - Results of the extracellular flux analysis of unprocessed and rehydrated conditions for both unexpressed and AfrLEA3m expressed cells. Metabolic analysis indicates desiccated and rehydrated AfrLEA3 expressed cells are comparable to unprocessed cells, whereas unexpressed cells have metabolic deficiencies.

Fig. 5.7A displays post processing outcomes for HepG2, unexpressed *Afr*LEA3m cells, and expressed *Afr*LEA3m cells. The two former samples had no immediate survival following spin drying treatment. The LEA3 expressed cells had a 92.3% immediate viability, as measured by membrane integrity. Fig. 5.8B displays growth for these treatment groups over a period of 7 days. Hep G2 cells which underwent no processing had relatively normal growth resulting in a

28-fold increase in cell number. The desiccated HepG2 and unexpressed *Afr*LEA3m cells had no immediate viability and thus had corresponding zero growth. The expressed *Afr*LEA3m cells had only 1.7-fold increase in cell number, only 6.1% of the unprocessed HepG2 cells. This would seem to indicate that while *Afr*LEA3m conferred protection in the immediate sense, the cells still sustained injury in some other way.

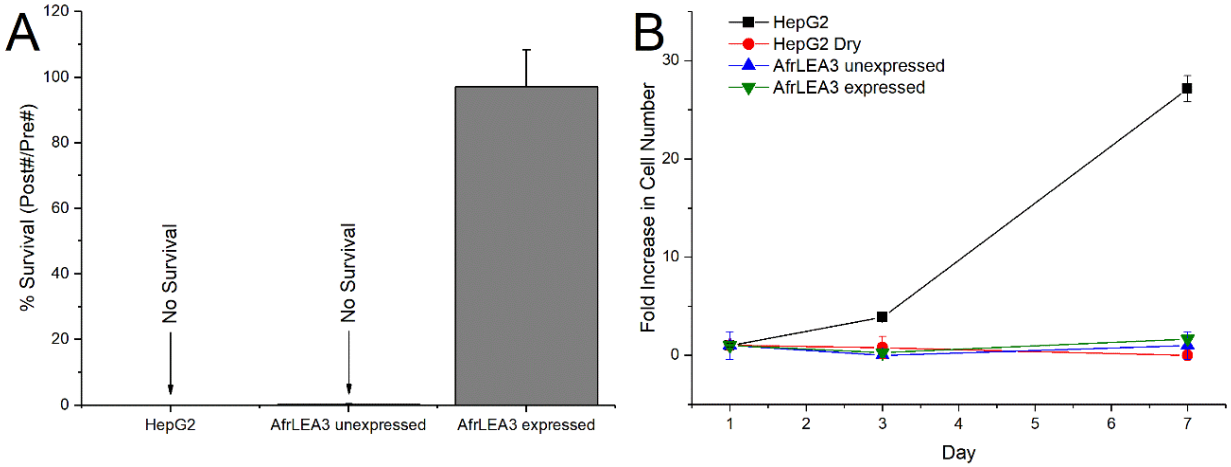

Figure 5.8: Viability of *Afr*LEA3m following desiccation - A) Percent survival, as measured by membrane integrity before dry processing and immediately after, for control HepG2 cells and HepG2 cells which have AfrLEA3 transfection, with (expressed) and without (unexpressed) doxycycline induction. Only cells which had AfrLEA3 inducement had any survival, with very good recovery at near 97%. B) Seven-day growth for HepG2 cells which were; control in physiological state (never dried), dried control cells, dried AfrLEA3 unexpressed cells, and dried AfrLEA3 expressed cells. Control cells not subjected to drying had a near 30-fold increase in cell number over 7 days. Dried control and unexpressed AfrLEA3 cells had no survival and no growth. AfrLEA3 cells had high initial recovery but only minimal growth for the 7-day period, ~1.7 fold increase.

5.4 Discussion

The potential of LEA group proteins for stabilization of biomedically relevant cells and tissues is well recognized, especially due to their prevalence in a diverse group of organisms which indicates broad protective mechanisms that are not cell or tissue type specific. Previously, it has been demonstrated that during acute desiccation events, e.g., spin drying, cells expressing *Afr*LEA3m have significantly improved survival rates compared to non-transgenic control cells. It was the objective of this study to present an analytical method for characterizing the protective benefits of *Afr*LEA3m during water stress in HepG2 cells.

From the data acquired from the hyperspectral scans (Fig. 5.3), several interesting differences are found between control cells and cells expressing *Afr*LEA3m. Both, fully hydrated and desiccated *Afr*LEA3m cells had significantly higher total protein contents than non-transfected control concentrations. The shift in amide intensities from the hydrated to the dry state carried an expected result, namely that the amide I signature were much decreased and amide III signatures showed strong increases. There was a significant increase in amide III levels of *Afr*LEA3m expressed cells over unexpressed cells, which was expected as the intrinsically disorder protein would display an increase in secondary structures upon desiccation. There is a distinct increase in amide II and III levels in the control HepG2 cells after desiccation and rehydration. This may be due to a lower concentration of CH2 components, making the normalized intensities appear larger. This has been observed previously and could indicate cellular damage. The *Afr*LEA3m expressing cells show amide levels closer to hydrated control cells. This lends support to the hypothesis that *Afr*LEA3m plays a protective role in desiccation events.

Extracellular flux analysis shows an apparent increase in mitochondrial poise of processed cells (which is a percent ratio of basal respiration to maximal respiration, which describes the

balance of mitochondrial output relative to maximum potential) compared to never dried control cells. There was an almost equivalent decrease in glycolytic poise for the same groups. This may be explained by Warburg effect related metabolism of the HepG2 cell line. After processing, acute energy demands of the cells may have been triggered and so mitochondrial activity was increased, with a proportional drop in normal glycolytic energy generation.

The normalized Raman amide II spectral ratios according to the cellular membrane show significantly higher values for *Afr*LEA3m expressed cells over unexpressed cells. This is most likely explained by residual increase of protein content.

The cytochrome c/mitochondrial poise parameter assists in providing a description of metabolic efficiency by coupling bioenergetic and spectroscopic data. *Afr*LEA3m expressed cells had a significantly lower ratio to that of unexpressed cells. This can describe that there is less cytochrome c in the cellular composition as derived from the Raman spectra with respect to the mitochondrial poise. A reasonable inference would be that the cells are therefore producing energy more efficiently, as for similar levels of metabolic output, there is less overall mitochondrial content, i.e., better efficiency. It should be noted that the cytochrome c peak used (1127 rel. 1/cm) was fairly weak, having a STN ratio of only ~3 and so future analysis will try to focus upon increasing STN for our target analyte. That stated, the spectrometabolic parameter establishes further support that cells which had protective *Afr*LEA3m protein, have better metabolic outcomes than cells which did not.

This study intended to provide evaluation of *Afr*LEA3m protective abilities in mammalian cells. Raman spectroscopy offers a powerful tool to aide in providing intrinsic chemical cellular information, such as α-helical structure. Coupled with bioenergetic assays, the analysis provided

within gives strong further support that using LEA-group proteins as a dry preservation strategy is eminently viable, particularly when coupled with existing complementary techniques.

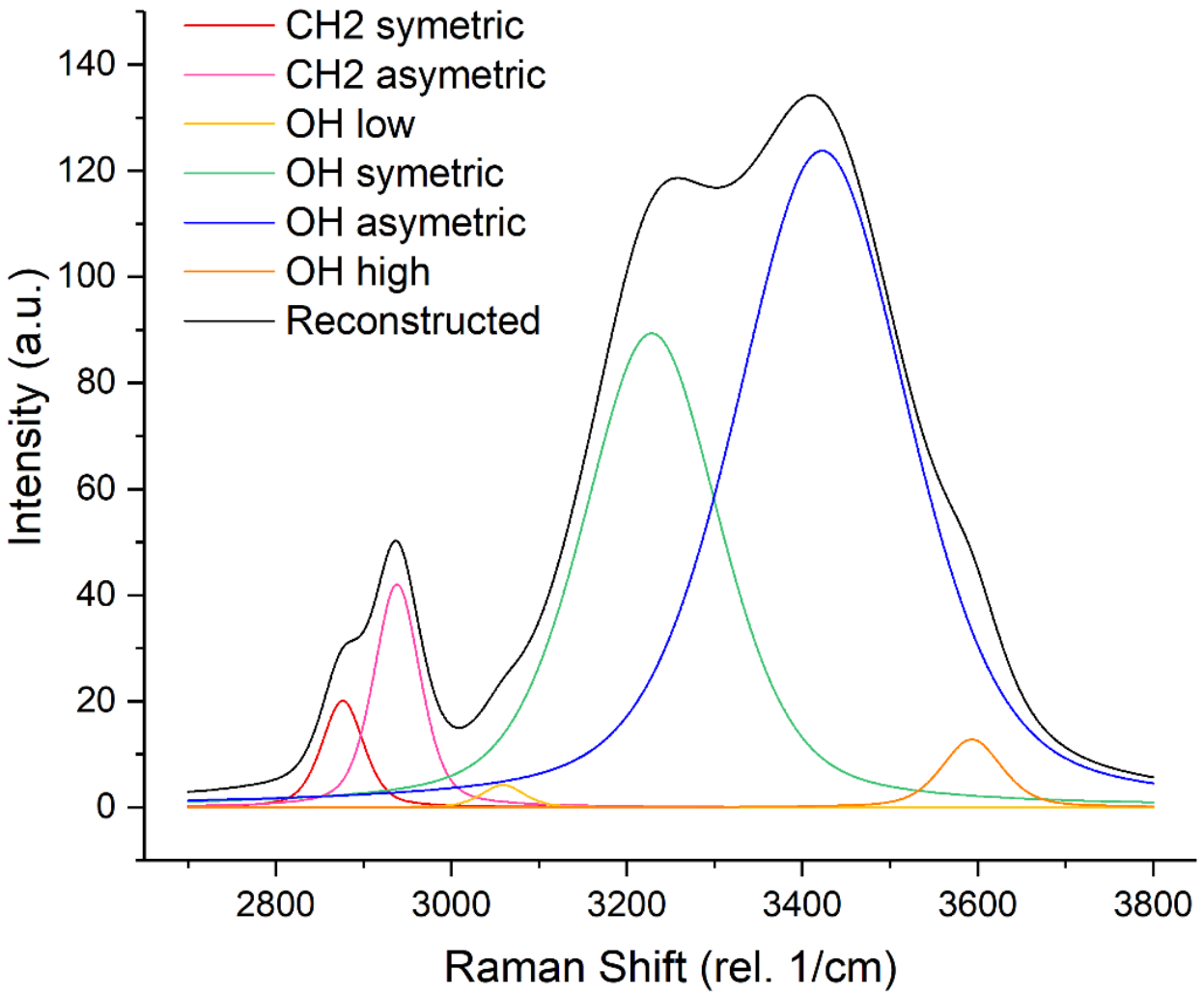

Figure 5.9: 6-peak Deconvolution of CH2- and OH- Stretching Bands - The CH2-stretching mode was deconvoluted into two primary bands, denoted as symmetric (red) and asymmetric (pink). The OH-stretching band was deconvoluted into 4 primary peaks, denoted as low (yellow), symmetric (green), asymmetric (blue), and high (orange). The black line is the convolution of these six bands. This allows for more targeted analysis for specific peaks.

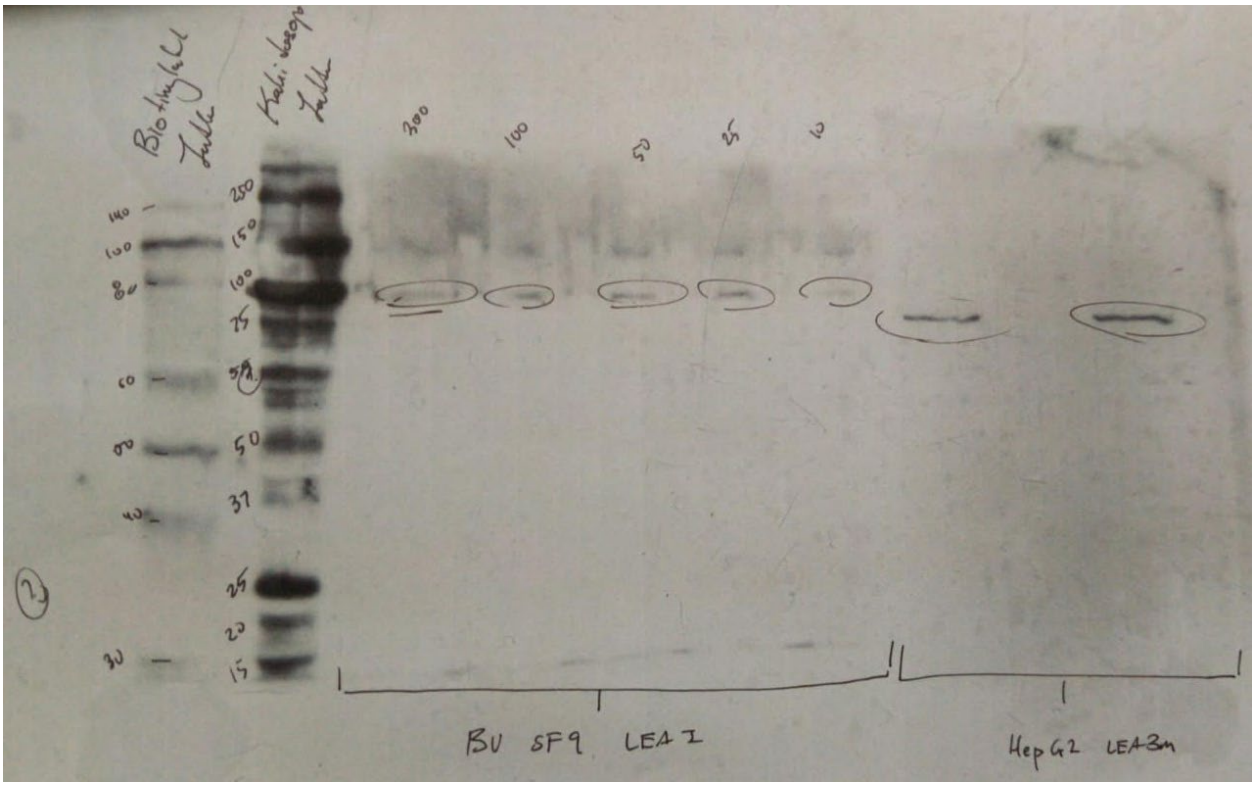

Figure 5.10: Western Blot to verify *Afr*LEA3m content in expressed cells

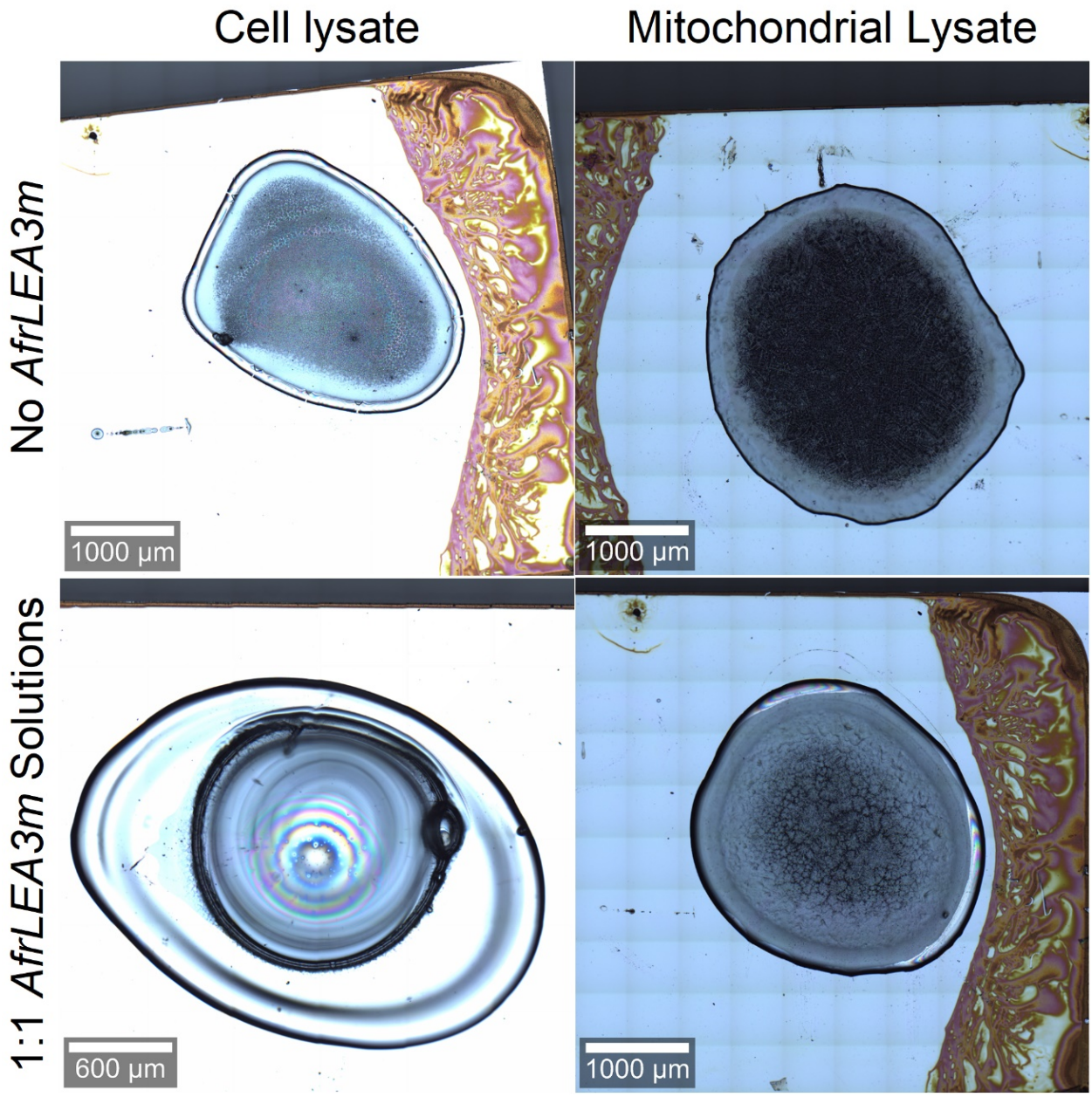

Figure 5.11: Dried droplets of cell and isolated mitochondrial lysates, with and without *AfrLEA3*m pure protein addition - 5 µL droplets were allowed to dry in sessile fashion on gold plates. Images are stitched brightfield captures using a 10x Zeiss objective.

Chapter 6

Spectrometabolic Response to Galactose Treatment

6.1 Introduction

A totalistic characterization methodology was undertaken for the metabolic response to replacement of glucose medium with an alternative hexose source, galactose. (Skolik, 2021) One key facet of the multi-level analysis technique is the spectrometabolic method described in the following.

An identic difference between primary cells and tumor derived cells is a metabolic proclivity towards lactate production in the latter. This can largely be attributed to a shift from mitochondrial oxidative phosphorylation to substrate level phosphorylation. (Warburg, 1956) It was originally thought that lower rates of respiration were due to mitochondrial dysfunction, but that has been shown to not necessarily be the case as many cancer cell lines have completely functional mitochondria. (Warburg, 1956; Moreno-Sanchez, 2007) From recent literature, it would seem it is not ATP, but biosynthetic precursors which control proliferation rates in tumor-origin cells. (Vander Heiden, 2009) An increase in glycolytic flux has corresponding increase in linked biosynthetic pathways. (Lunt, 2011; DeBeradinis, 2008) As an example, the pentose phosphate pathway has genesis in the glycolysis intermediate metabolite glucose-6-phosphate, which sees elevated activity in tumor origin cells. The pentose phosphate pathway in turn creates biosynthetic precursors, e.g., NADPH, for functions including lipid synthesis and maintenance of redox homeostasis. (Jiang, 2014; Patra, 2014) However, the disparate metabolic regimes between tumor

origin cells and primary cells are often not considered. It is shown in the following that replacement of primary hexose source from glucose to galactose reintroduces a metabolic modality to cancerous cells which is more akin to their primary cell counterparts. This has the obvious implication of improving the physiological relevance for tumor origin cells in biomedical research. It also carries with it the potential for insights into therapeutics targeting cancers specifically due to their metabolic poise.

It has been shown that for certain immortalized cell lines, a metabolic shift favoring oxidative phosphorylation occurs when switching form glucose to galactose. (Rossignol, 2004) An increase in oxygen consumption at the mitochondria, along with decreased lactate production indicates this substrate shift decreases glycolytic flux while increasing ATP production in the mitochondria. (Gohil, 2010; Grimm, 2017) There is also proof that cells incubated with galactose replacement have increased production of proteins necessary for oxidative phosphorylation as well as being more susceptible to mitochondria dysfunction and toxins. (Marroquin, 2007; Arroyo, 2016; Bayona-Bafaluy, 2011) Overall, the effects of galactose incubation to tumor derived cells have been insufficiently characterized.

Both glucose and galactose are converted to glucose-6-phosphate after uptake into the cell by means of solute carrier 2A proteins or sodium dependent hexose transporters. (Augustin 2018; Ghezzi, 2018; Tahrani, 2013) However, glucose accomplishes this in a single enzymatic step while galactose requires four reactions of the Leloir pathway. (Holden, 2013) ATP production via catabolism of either sugar has similar potential yields, and both produce glucose-6-phosphate which can be utilized in glycolysis or the pentose phosphate pathway. (Frey, 1996)

Herein, the physiological effects of galactose replacement on tumor derived cell lines are characterized using hepatocellular carcinoma (HepG2) cell line. These are of particular utility due

to their high metabolic plasticity and widespread use in hepatoxicity assessment. (Soldatow, 2013; Tolosa, 2013) It is shown herein that galactose replacement decreases both mitochondrial and cytosolic NAD+/NADH ratios against cells maintained in glucose culture. This is suggestive that such a substrate replacement could normalize HepG2 metabolism to a more typically found primary hepatocyte metabolic poise, in order to increase physiological relevancy in biomedical research utilizing these cells for biomedical application.

6.2 Materials and Methods

6.2a Chemicals

Chemicals acquired for solution preparations were of the highest purity and purchased either from Sigma-Aldrich (St. Louis, MO) or Thermo Fischer Scientific (Waltham, MA). Reagents for extracellular flux analysis were acquired from Seahorse Bioscience (Billerica, MA).

6.2b Cell Culture

Human hepatocellular carcinoma cells (HepG2) were purchased from the American Type Culture Collection (ATCC, Manassas, VA) and cultured in T-75 flasks (Corning Company, Corning, NY). Cells were grown in media composed of glucose-free Dulbecco's modified eagles medium (DMEM) (Thermo Fischer Scientific, Waltham, MA) supplemented with 2 mM glutamine (VWR, West Chester, PA), 1 mM pyruvate (Corning Company, Corning, NY), 10 mM glucose (Thermo Fischer Scientific, Waltham, MA), and 10% dialyzed fetal bovine serum (12-14 kDa) (Atlanta Biologicals Inc., Flowery Branch, GA). Depending on experimental group, either 10 mM glucose was substituted with 10 mM galactose (Thermo Fischer Scientific, Waltham, MA)

(galactose medium) or non-dialyzed FBS (Atlanta Biologicals Inc., Flowery Branch, GA) was substituted for dialyzed FBS to culture cells. All cells were maintained in a humidified atmosphere at 5% CO_2 and 95% air at 37°C. Culture medium was renewed every two days and cells were passaged before reaching 90% confluency. To subculture, cells were dissociated from the culture flasks using 0.25% trypsin and 1 mM EDTA in a balanced salt solution (Thermo Fischer Scientific, Waltham, MA), centrifuged at 200 x g for 5 min.

6.2c Extracellular Acidification Rates

To characterize extracellular acidification rates (ECAR) of HepG2 cells, an XFp Seahorse flux analyzer (Agilent Technologies, Santa Clara, CA) was used. The day prior to ECAR measurements, cells were placed into glucose-containing medium in standard microwell plates at a seeding density of 2 x 10^4 cells per well. ECAR measurements were collected using the Seahorse standard protocol and cartridge sensors were hydrated with XF calibrant overnight. On the day of the experiment, medium was aspirated and replaced with the experimental medium. Cells were contained in an incubator with hydrated air at 37°C for 1 hr for CO_2 gas removal. Following incubation, ten measurements were taken in three minute intervals. The lactate dehydrogenase inhibitor GSK 2837808A (Torcis, Bristol, United Kingdom) was used at a final injection concentration of 20 μM. The plate was mixed and analyzed before and after injections to obtain steady ECAR values.

6.2d Raman Microspectroscopy

HepG2 cells were grown for 4 weeks either in glucose or galactose medium before conducting Raman microspectroscopic experiments. Spatially correlated Raman microspectroscopic measurements were acquired using a customized confocal microscope (Zeiss Corp., Oberkochen, Germany) and Raman spectrometer combination (UHTS 300, WITec Instruments Corp., Ulm, Germany) connected to a CCD camera (Andor Technology, Belfast, Ireland). A 532 nm solid-state laser calibrated to 20 mW was used for excitation and a custom 50X objective for observation (Mitutoyo, Sakado Japan). The changes in the spectral signature from the intracellular space were analyzed using a hyperspectral molecular analysis technique. Spectral arrays were collected using a spatial dimension of 30 μm × 30 μm with a spectral dimension of 90 x 90 pixels (n = 3). Each array of scans was collected using an integration time of 0.5 s. Typical background and substrate subtractions were employed, using WITec Project 5 and Peakfit v4 software. Principal component analysis (PCA) was used to reduce the dimensionality of the collected spectral data arrays into principal components (PCs) and then reconstructed according to a signal-to-noise threshold for selecting PC number. Following noise reduction using PCA, hierarchal cluster analysis was used to construct average spectral signatures for regional components of the cellular hyperspectral arrays based on significant components. Brightfield images were taken to locate desired cells. Following acquisition of hyperspectral Raman array scans, a cluster analysis was performed to yield discreet binned spectral groups. Each cluster produces an averaged Raman spectrum (755 rel. 1/cm is assigned to cytochrome-c, 1012 rel. 1/cm is assigned to NAD^+, 1594 rel. 1/cm is assigned to NADH, and the wide band centered at 2940 rel. 1/cm represents CH2 stretching mode, used primarily for self-normalization). The wavenumber

assignment for NAD^+, NADH, and cytochrome c mentioned here were verified by collection of spectral signatures from pure reagents, respectively.

6.2e Statistical Analysis

Data was analyzed using an unpaired two-tailed t-test, or one-way analysis of variance (ANOVA) test. Statistical analysis was evaluated using GraphPad Prism 8.4 software (GraphPad Software Inc., San Diego, CA).

6.3 Results

Metabolomic analysis reveals a statistically insignificant trend towards a lower NAD^+/ NADH redox ratio in cultured cells which have undergone galactose replacement. However, these bulk measurements do not allow for acquisition of subcellular resolution and so the Raman spectrometabolic technique was developed to characterize single cell redox ratios. The compartment specific measurements are initialized by first scanning pure NAD compounds. Then identification of these signatures in single aqueous HepG2 cells through confocal Raman microspectroscopy to independently monitor the mitochondrial and cytoplasmic NAD^+/NADH redox ratios (Fig. 6.1A-C) was established. Cytochrome-*c* was used as the signature to identify mitochondrial regions, calculate the average spectra for these regions, and ultimately allow for comparisons to be made between the redox ratios measured in both the mitochondrial and cytoplasmic compartments. The technique accuracy was tested by introduction of the lactate dehydrogenase inhibitor, GSK 2837808A (20 μM), in order to prevent oxidation of NADH to NAD^+ in the cytosolic environment while at the same time extracellular acidification rates (ECAR) were acquired to confirm the LDH inhibition. Before LDH inhibition, galactose cultured cells had

a 169 ± 8.2% lower ECAR compared to the glucose control. LDH inhibition significantly lowered ECAR in glucose by 145 ± 10% and by 37 ± 8% for galactose cultured cells and resulted in a comparative 51 ± 10% difference of ECAR in the presence of the LDH inhibitor (Fig. 6.1D). Raman microspectroscopy measured the cytoplasmic NAD^+/ NADH redox ratio for HepG2 cells cultured with galactose was 26 ± 6% lower in absence of the LDH inhibitor (Fig. 6.1E). After LDH inhibition, the cytoplasmic NAD^+/NADH redox ratio decreased by 43 ± 7% in glucose and 32 ± 4% in galactose cultured cells. Despite the redox ratios decreasing for both glucose and galactose conditions upon injection of the LDH inhibitor, a significantly lower redox ratio was shown for galactose treated cells compared to glucose cultured cells. As aforementioned, the mitochondrial NAD^+/NADH ratio was assessed in both glucose and galactose substituted cells via colocalization with the cytochrome-c signature. The mitochondrial redox ratio was lower for both conditions when compared to the cytoplasmic redox ratios. Cells cultured with galactose were shown to have a 20 ± 6% lower mitochondrial NAD^+/NADH ratio compared to the glucose control cells. (Fig. 6.1F)

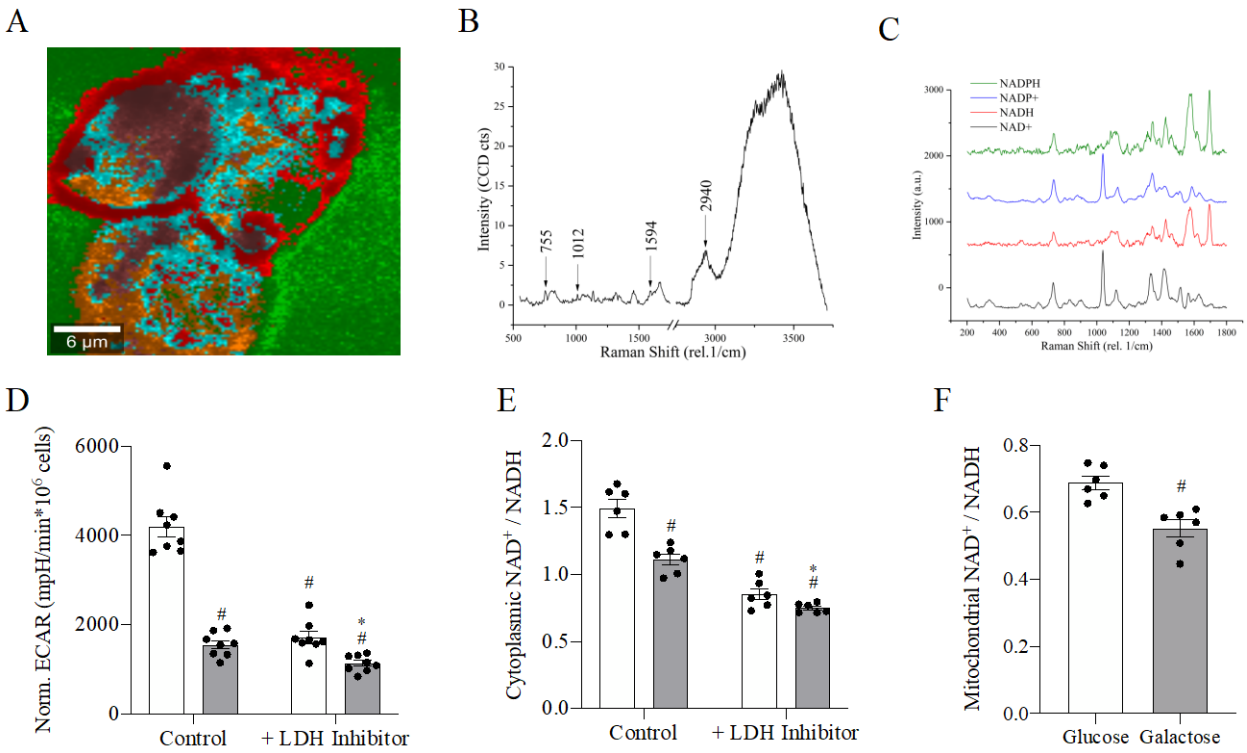

Figure 6.1: Galactose shifts cytoplasmic NAD(H) redox ratio - Acquisition of Raman spectra of pure NAD^+, NADH, $NADP^+$, and NADPH compounds and identification in HepG2 cells. The fingerprint region of each of each of the compounds were used to spatially correlated with the intracellular distribution of the compounds. A) Representative Raman spectra of a cluster average. B) Intensity of 755 rel. 1/cm peak, representing cytochrome C, increasing as function of cluster degree. C) Cascade graph of Raman spectra for four related NAD compounds. D) Extracellular acidification of HepG2 cells cultured with glucose or galactose in presence or absence of the LDH inhibitor, GSK 2837808A (20 µM). #Indicates statistically significant differences compared to glucose control. *Indicates statistically significant between glucose and galactose condition in presence of LDH inhibitor (One-way ANOVA, $p < 0.05$, $n = 8$, average ± SEM). E) Cytoplasmic NAD^+/NADH ratio obtained from Raman spectra for HepG2 cells cultured with glucose or galactose in presence or absence of GSK 2837808A (20 µM). #Indicates statistically significant differences compared to glucose control. *Indicates statistically significant between glucose and galactose condition in presence of LDH inhibitor. (One-way ANOVA, $p < 0.05$, $n = 6$, average ± SEM). F) Mitochondrial NAD^+/NADH obtained from Raman spectra for HepG2 cells cultured in glucose or galactose. #Indicates statistically significant differences compared to glucose control. (Unpaired t-test, $p < 0.05$, $n = 6$, average ± SEM).

6.4 Discussion

Here it is demonstrated that it is possible to shift the metabolic poise of tumor origin HepG2 cells to more closely mirror their primary hepatocyte counterparts via the replacement of glucose with galactose substrate source. While there have been some studies done into the increased oxidative phosphorylation activities of galactose incubated cells, the overall implications for global metabolic pathways has been insufficiently explored. (Aguer, 2011; Dott, 2014) Therefore, to investigate the subcellular localized involvement of the redox state to overall metabolic poise, the Raman spectrometabolic technique was used to evaluate the compartmentalized NAD+/NADH ratios. This characterization technique allowed for effective differentiation of impact on global metabolic pathways based on the hexose source used.

Admittedly, galactose replacement as a technique to shift respiration profiles to more close match primary cells may only be limited to specific cell lines, such as the HepG2s evaluated here. It is thought that galactose serves as a necessary substrate source in a glucose free environment. While glycolysis pathways produce equal ATP yields for both glucose and galactose, it has been posited that galactose cultured cells likely derive most ATP form catabolism of glutamine and pyruvate. (Reitzer, 1979) It is hypothesized that galactose is a critical carbon contributor to the pentose phosphate pathway, which is also surmised to likely be the primary metabolic pathway for cells cultured in a galactose medium, over the TCA cycle.

The NAD+/NADH ratio can be used as a prime metric for metabolic appraisal. The NAD+/NADH ratio is responsible for the regulation of flux through many different metabolic pathways. (Hosios, 2018) It has been thought that high NAD+/NADH ratios will typically facilitate cell proliferation through flux sustainment via oxidative biosynthetic pathways. (Diehl, 2019; Gui, 2016; Luengo, 2017; Titov, 2016) One major limitation of traditional metabolomic analysis

techniques is that it can only evaluate total NAD compound levels. However, NAD concentration, NAD synthesis, and the overall redox ratios vary drastically with subcellular localization. (Cambronne, 2016) As an example, NAD levels in the mitochondria are largely unaffected by the depletion of NAD compounds in the cytoplasm, and NAD concentration are somewhere between two and tenfold greater in the mitochondria. (Alano, 2007; Pittelli, 2010; Tischler, 1977; Yang, 2007) Also, NAD+/NADH ratios in the mitochondria can range anywhere from 2 – 8, while the redox ratio occurring in the cytoplasm ranges from 0.1 – 600. (Lin, 2003; Sun, 2012; Williamson, 1967)

Employing the Raman spectroscopy, localized spectrometabolic analysis was able to be carried out. It was observed that there was lower NAD+/NADH ratios in the mitochondria, compared to the cytoplasm for the HepG2 model system investigated, for both glucose and galactose treatment groups. However, the cells which had galactose replaced culture conditions had a lower NAD+/NADH ratio for both mitochondrial and cytoplasmic regions. So, the shift in metabolic poise occurs across the entirety of the cell upon replacement of glucose with galactose. The NAD+/NADH ratio in the cytoplasm is regulated primarily by the conversion of pyruvate to lactate via lactate dehydrogenase. This lactate dehydrogenase reaction is about twice as fast than general flux rates via glycolysis, which results in fast regeneration of NAD+ when pyruvate concentrations are high. (Sun, 2012) An increased metabolic flux via lactate dehydrogenase is seen in glucose conditioned HepG2 cells over those which had only galactose incubation, resulting in higher NAD+/NADH ratios in the cytoplasm. An increase in NAD+ bioavailability might allow for sustained glycolytically linked ATP generation, as well as facilitating metabolic flux for oxidative pathways. (Diehl, 2019) Regardless of this possibility, it can be said that prominent

metabolic shift which corresponds to altering hexose source from glucose to galactose in HepG2 cells may lower overall compartmentalized NAD+/NADH ratios.

This study presents a highly utilizable technique in spectrometabolic characterization. The utility shown here was to evaluate the substitution of hexose source to better reflect the metabolic modalities of primary hepatocytes. Leveraging the microspectroscopic features of the analysis, redox ratios were able to be quantified for independent intracellular compartments, notably the mitochondria and the cytoplasm. Such analysis regimes can be used to explore cancer remediation strategies, and to fully explore more physiologically relevant analytical strategies.

Chapter 7

Future Research and Conclusion

The research contained in the previous pages serves as the stage for a technique which has amazing potential for great public health benefits. The standard premise of the technique is such; begin by characterizing the bioenergetics of model mammalian cells using standard metabolic profiling. Then, implement Raman microspectroscopic global analysis to elucidate all internal biochemical signatures quantitatively. Then, create the bridging analysis method to connect the spectroscopic data towards the standardized metabolic data. Use this spectrometabolic analysis technique as a framework to then evolve into more advanced, optimal techniques. Finally, test this model in a diagnostic, if not clinical, role to validate novel technique efficacy. This is the hopeful proposed course for the methods which have been initially tested herein.

Going forward, a key technique towards optimization that has seen exponentially increased use is that of big data, in neural networks/artificial intelligence. Computing power is becoming increasingly cheap and common, and strategies for leveraging computer analysis of monstrous amounts of data is becoming a standardized notion. This is highly relevant to the works completed and to the future path proposed. For the type of information that Raman microspectroscopy provides, particularly with hyperspectral chemical imaging, it is well suited for the setting of a neural network. The layers of information that spectroscopy is entwined with may seem burdensome when dealing with it case by case, but eventually it can be imagined to be an immense asset to advanced systems. Imagine a clinical diagnostic procedure whereby a biopsy sample is

drawn, fed into a spectroscopic analyzer, the raw data from which enters a conditioned neural network system, and one of several analysis outcomes provided. This can be seen as a yes/no operator for, “Is this sample cancer tissue?”. Or for evaluating metabolic flux for prescreening neurodegenerative disorders. To this end, through this work, it has been demonstrated that spectroscopic insights into not only metabolic changes were made, but other compounding variables, in a unified analysis methodology. This includes the effect of potential pharmaceutical candidates on not only the overall metabolism but also the compartmentalized subcellular structures in model adrenal gland cells. The implication of reactive oxygen species induced toxicity complicity was evident by multiple techniques, namely; microspectroscopy, standard growth studies, metabolic profiling, and reactive oxygen species quantification assays. In the future, only the spectrometabolic technique would ideally be employed, saving valuable time and efforts.

Another interesting topic evaluated was that this technique demonstrated that spectroscopy could illuminate the subcellular machinations of a protein conforming to a predetermined secondary structure to impart stability upon a desiccation event. This is a biomimetic strategy taken from nature, who has carefully refined so many extraordinary techniques through the eons. However, humanity in its own cleverness has created the tools of CRISPR/Cas9 and other advanced gene editing tools to, with surgical precision, alter the possibilities of life. With strategies such as imparting desiccation tolerance to animals, or even humans on the (likely distant) horizon, the need to have effective tools for equally precise analysis must be developed and refined. The spectrometabolic techniques described can simultaneously examine the protein structure, metabolism, associated potential illnesses, and even more inherent features as research progresses. Such global analysis may be particularly beneficial to cellular analysis since cellular

dynamics are often interlocked in effects and more univariate analysis forms can miss one while probing another.

The days when one could master the knowledge of all life's domains has long since passed. The level of speciality one must have to break through scientific boundaries is extraordinary. The ironic feature of this condition is that so many of the most profound insights, inventions, and discoveries are had when non-associated areas of research are brought together in academic fusion. Furthermore, esoteric pursuits can be exceptionally interesting but relatively fruitless. There must be a human component for meaning to be instilled. And so, the proposed technique discussed previously is meant to be a bridge between several disciplines for the betterment of the human condition. There is a high hope that some meaningful fruits can be had from the research provided, even if only to some small part of humanity.

Bibliography

Acker, J. P. (2007). Biopreservation of cells and engineered tissues. In K. Lee & D. Kaplan (Eds.), *Tissue Engineering II: Basics of Tissue Engineering and Tissue Applications* (pp. 157–187). Springer.

Aguer, C., Gambarotta, D., Mailloux, R. J., Moffat, C., Dent, R., McPherson, R., & Harper, M. E. (2011). Galactose enhances oxidative metabolism and reveals mitochondrial dysfunction in human primary muscle cells. *PloS ONE*, *6*(12), e28536.

Alano, C. C., Tran, A., Tao, R., Ying, W., Karliner, J. S., & Swanson, R. A. (2007). Differences among cell types in NAD+ compartmentalization: A comparison of neurons, astrocytes, and cardiac myocytes. *Journal of Neuroscience Research*, *85*(15), 3378-3385.

Andersson, G. E., Karlberg, O., Canbäck, B., & Kurland, C. G. (2003). On the origin of mitochondria: A genomics perspective. *Philosophical Transactions of the Royal Society of London. Series B: Biological Sciences*, *358*(1429), 165-179.

Arroyo, J. D., Jourdain, A. A., Calvo, S. E., Ballarano, C. A., Doench, J. G., Root, D. E., & Mootha, V. K. (2016). A genome-wide CRISPR death screen identifies genes essential for oxidative phosphorylation. *Cell Metabolism*, *24*(6), 875-885.

Augustin, R., & Mayoux, E. (2018). Mammalian solute carrier families SLC2 and SLC5: Facilitative and active transport of hexoses and polyols. In R. D. Wells, J. S. Bond, J. P. Klinman, B. B. S. Masters, & E. Bell (Eds.), *Molecular Life Sciences: An Encyclopedic Reference* (pp. 627–651). Springer.

Ayers, G. R., & Dainty, J. C. (1988). Iterative blind deconvolution method and its applications. *Optics Letters*, *13*(7), 547-549.

Barbeau, A. (1962). The pathogenesis of Parkinson's disease: A new hypothesis. *Canadian Medical Association Journal*, *87*(15), 802.

Bayona-Bafaluy, M. P., Sánchez-Cabo, F., Fernández-Silva, P., Pérez-Martos, A., & Enríquez, J. A. (2011). A genome-wide shRNA screen for new OxPhos related genes. *Mitochondrion*, *11*(3), 467-475.

Begley, R. F., Harvey, A. B., & Byer, R. L. (1974). Coherent anti-Stokes Raman spectroscopy. *Applied Physics Letters*, *25*(7), 387-390.

Bertler, Å., & Rosengren, E. (1959). Occurrence and distribution of dopamine in brain and other tissues. *Experientia*, *15* (1), 10-11.

Bonora, M., Patergnani, S., Rimessi, A., De Marchi, E., Suski, J.M., Bononi, A., Giorgi, C., Marchi, S., Missiroli, S., Poletti, F. & Wieckowski, M.R., (2012). ATP synthesis and storage. *Purinergic Signalling*, *8*(3), 343-357.

Boswell, L. C., & Hand, S. C. (2014). Intracellular localization of group 3 LEA proteins in embryos of *Artemia franciscana*. *Tissue and Cell*, *46*(6), 514-519.

Boswell, L. C., Moore, D. S., & Hand, S. C. (2014). Quantification of cellular protein expression and molecular features of group 3 LEA proteins from embryos of *Artemia franciscana*. *Cell Stress and Chaperones*, *19*(3), 329-341.

Boucher, V., Buitink, J., Lin, X., Boudet, J., Hoekstra, F. A., Hundertmark, M., Renard, D. & Leprince, O., (2010). MtPM25 is an atypical hydrophobic late embryogenesis-abundant protein that dissociates cold and desiccation-aggregated proteins. *Plant, Cell & Environment*, *33*(3), 418-430.

Boyle, W. S., & Smith, G. E. (1970). Charge coupled semiconductor devices. *Bell System Technical Journal*, *49*(4), 587-593.

Cambronne, X.A., Stewart, M.L., Kim, D., Jones-Brunette, A.M., Morgan, R.K., Farrens, D.L., Cohen, M.S. & Goodman, R.H., (2016). Biosensor reveals multiple sources for mitochondrial NAD+. *Science*, *352*(6292), 1474-1477.

Capaldi, R. A., & Aggeler, R. (2002). Mechanism of the F1F0-type ATP synthase, a biological rotary motor. *Trends in Biochemical Sciences*, *27*(3), 154-160.

Carlsson, A. (1959). The occurrence, distribution and physiological role of catecholamines in the nervous system. *Pharmacological Reviews*, *11*(2), 490-493.

Chakrabortee, S., Boschetti, C., Walton, L. J., Sarkar, S., Rubinsztein, D. C., & Tunnacliffe, A. (2007). Hydrophilic protein associated with desiccation tolerance exhibits broad protein stabilization function. *Proceedings of the National Academy of Sciences*, *104*(46), 18073-18078.

Chakraborty, N., Chang, A., Elmoazzen, H., Menze, M. A., Hand, S. C., & Toner, M. (2011). A spin-drying technique for lyopreservation of mammalian cells. *Annals of Biomedical Engineering*, *39*(5), 1582-1591.

Chakraborty, N., Menze, M. A., Elmoazzen, H., Vu, H., Yarmush, M. L., Hand, S. C., & Toner, M. (2012). Trehalose transporter from African chironomid larvae improves desiccation tolerance of Chinese hamster ovary cells. *Cryobiology*, *64*(2), 91-96.

Dagley, S., & Nicholson, D. E. (1970). *An Introduction to Metabolic Pathways*. Blackwell Scientific Publications.

DeBerardinis, R. J., Lum, J. J., Hatzivassiliou, G., & Thompson, C. B. (2008). The biology of cancer: Metabolic reprogramming fuels cell growth and proliferation. *Cell Metabolism*, *7*(1), 11-20.

Diehl, F. F., Lewis, C. A., Fiske, B. P., & Vander Heiden, M. G. (2019). Cellular redox state constrains serine synthesis and nucleotide production to impact cell proliferation. *Nature Metabolism*, *1*(9), 861-867.

Dott, W., Mistry, P., Wright, J., Cain, K., & Herbert, K. E. (2014). Modulation of mitochondrial bioenergetics in a skeletal muscle cell line model of mitochondrial toxicity. *Redox Biology*, *2*, 224-233.

Dure III, L., Greenway, S. C., & Galau, G. A. (1981). Developmental biochemistry of cottonseed embryogenesis and germination: Changing messenger ribonucleic acid populations as shown by in vitro and in vivo protein synthesis. *Biochemistry*, *20*(14), 4162-4168.

Edwards, A. W., & Cavalli-Sforza, L. L. (1965). A method for cluster analysis. *Biometrics*, 362-375.

Forno, L. S. (1988). The neuropathology of Parkinson's disease. In F. Hefti & W. J. Weiner (Eds.), *Progress in Parkinson Research* (pp. 11–21). Springer.

Fowler, A., & Toner, M. (2006). Cryo-injury and biopreservation. *Annals of the New York Academy of Sciences*, *1066*(1), 119-135.

Frey, P. A. (1996). The Leloir pathway: A mechanistic imperative for three enzymes to change the stereochemical configuration of a single carbon in galactose. *The FASEB Journal*, *10*(4), 461-470.

Further Consolidated Appropriations Act, Public Law (P.L.) 116-94, (2020).

Ghezzi, C., Loo, D. D., & Wright, E. M. (2018). Physiology of renal glucose handling via SGLT1, SGLT2 and GLUT2. *Diabetologia*, *61*(10), 2087-2097.

Gillette, J. R., Mitchell, J. R., & Brodie, B. B. (1974). Biochemical mechanisms of drug toxicity. *Annual Review of Pharmacology*, *14*(1), 271-288.

Gogoi, S., Antonio, T., Rajagopalan, S., Reith, M., Andersen, J., & Dutta, A. K. (2011). Dopamine D2/D3 agonists with potent iron chelation, antioxidant and neuroprotective properties: Potential implication in symptomatic and neuroprotective treatment of Parkinson's disease. *ChemMedChem*, *6*(6), 991-995.

Gohil, V.M., Sheth, S.A., Nilsson, R., Wojtovich, A.P., Lee, J.H., Perocchi, F., Chen, W., Clish, C.B., Ayata, C., Brookes, P.S. & Mootha, V.K., (2010). Nutrient-sensitized screening for drugs that shift energy metabolism from mitochondrial respiration to glycolysis. *Nature Biotechnology*, *28*(3), 249-255.

Gray, M. W., Burger, G., & Lang, B. F. (2001). The origin and early evolution of mitochondria. *Genome Biology*, *2*(6), 1-5.

Gremlich, H.-U., & Yan, B. (Eds.). (2001). *Infrared and Raman Spectroscopy of Biological Materials* (Vol. 24, Ser. Practical Spectroscopy). Marcel Dekker.

Grimm, D., Altamirano, L., Paudel, S., Welker, L., Konkle, M. E., Chakraborty, N., & Menze, M. A. (2017). Modulation of cellular energetics by galactose and pioglitazone. *Cell and Tissue Research*, *369*(3), 641-646.

Gui, D.Y., Sullivan, L.B., Luengo, A., Hosios, A.M., Bush, L.N., Gitego, N., Davidson, S.M., Freinkman, E., Thomas, C.J. and Vander Heiden, M.G., (2016). Environment dictates dependence on mitochondrial complex I for NAD+ and aspartate production and determines cancer cell sensitivity to metformin. *Cell Metabolism*, *24*(5), 716-727.

Hand, S. C., & Menze, M. A. (2015). Molecular approaches for improving desiccation tolerance: Insights from the brine shrimp *Artemia franciscana*. *Planta*, *242*(2), 379-388.

Hayez, V., Guillaume, J., Hubin, A., & Terryn, H. (2004). Micro-Raman spectroscopy for the study of corrosion products on copper alloys: Setting up of a reference database and studying works of art. *Journal of Raman Spectroscopy*, *35*(8-9), 732-738.

Hernandez Guevara H, Hervas Soriano F, Tuebke A, Dosso M, Vezzani A, Amoroso S, & Grassano N. The 2014 EU Industrial R&D Investment Scoreboard. (pp. 47-55) EUR 26903. Publications Office of the European Union; 2014.

Holden, H. M., Rayment, I., & Thoden, J. B. (2003). Structure and function of enzymes of the Leloir pathway for galactose metabolism. *Journal of Biological Chemistry*, *278*(45), 43885-43888.

Hornykiewicz, O. (1989). Ageing and neurotoxins as causative factors in idiopathic Parkinson's disease—a critical analysis of the neurochemical evidence. *Progress in Neuro-Psychopharmacology and Biological Psychiatry*, *13*(3-4), 319-328.

Hosios, A. M., & Vander Heiden, M. G. (2018). The redox requirements of proliferating mammalian cells. *Journal of Biological Chemistry*, *293*(20), 7490-7498.

Hoult, D. I., & Bhakar, B. (1997). NMR signal reception: Virtual photons and coherent spontaneous emission. *Concepts in Magnetic Resonance: An Educational Journal*, *9*(5), 277-297.

Hunault, G., & Jaspard, E. (2010). LEAPdb: A database for the late embryogenesis abundant proteins. *BMC Genomics*, *11*(1), 1-9.

Iturriaga, G. (2008). The LEA proteins and trehalose loving couple: A step forward in anhydrobiotic engineering. *Biochemical Journal*, *410*(2), 1-2.

Jellinger, K., Paulus, W., Grundke-Iqbal, I., Riederer, P., & Youdim, M. B. H. (1990). Brain iron and ferritin in Parkinson's and Alzheimer's diseases. *Journal of Neural Transmission-Parkinson's Disease and Dementia Section*, *2*(4), 327-340.

Jiang, P., Du, W., & Wu, M. (2014). Regulation of the pentose phosphate pathway in cancer. *Protein & Cell*, *5*(8), 592-602.

Johnson, M., Antonio, T., Reith, M. E., & Dutta, A. K. (2012). Structure–activity relationship study of N^6-(2-(4-(1*H*-indol-5-yl)piperazin-1-yl)ethyl)-N^6-propyl-4,5,6,7-tetrahydrobenzo[d]thiazole-2, 6-diamine analogues: Development of highly selective D3 dopamine receptor agonists along with a highly potent D2/D3 agonist and their pharmacological characterization. *Journal of Medicinal Chemistry*, *55*(12), 5826-5840.

Langston, J. W., Ballard, P., Tetrud, J. W., & Irwin, I. (1983). Chronic Parkinsonism in humans due to a product of meperidine-analog synthesis. *Science*, *219*(4587), 979-980.

LeBlanc, B. M., Le, M. T., Janis, B., Menze, M. A., & Hand, S. C. (2019). Structural properties and cellular expression of AfrLEA6, a group 6 late embryogenesis abundant protein from embryos of *Artemia franciscana*. *Cell Stress and Chaperones*, *24*(5), 979-990.

Lesage, S., & Brice, A. (2009). Parkinson's disease: From monogenic forms to genetic susceptibility factors. *Human Molecular Genetics*, *18*(R1), R48-R59.

Li, C., Biswas, S., Li, X., Dutta, A. K., & Le, W. (2010). Novel D3 dopamine receptor-preferring agonist D-264: Evidence of neuroprotective property in Parkinson's disease animal models induced by 1-methyl-4-phenyl-1, 2, 3, 6-tetrahydropyridine and lactacystin. *Journal of Neuroscience Research*, *88*(11), 2513-2523.

Li, S., Chakraborty, N., Borcar, A., Menze, M. A., Toner, M., & Hand, S. C. (2012). Late embryogenesis abundant proteins protect human hepatoma cells during acute desiccation. *Proceedings of the National Academy of Sciences*, *109*(51), 20859-20864.

Lin, S. J., & Guarente, L. (2003). Nicotinamide adenine dinucleotide, a metabolic regulator of transcription, longevity and disease. *Current Opinion in Cell Biology*, *15*(2), 241-246.

Linert, W., & Jameson, G. N. L. (2000). Redox reactions of neurotransmitters possibly involved in the progression of Parkinson's Disease. *Journal of Inorganic Biochemistry*, *79*(1-4), 319-326.

Luengo, A., Gui, D. Y., & Vander Heiden, M. G. (2017). Targeting metabolism for cancer therapy. *Cell Chemical Biology*, *24*(9), 1161-1180.

Lunt, S. Y., & Vander Heiden, M. G. (2011). Aerobic glycolysis: Meeting the metabolic requirements of cell proliferation. *Annual Review of Cell and Developmental Biology*, *27*, 441-464.

Marroquin, L. D., Hynes, J., Dykens, J. A., Jamieson, J. D., & Will, Y. (2007). Circumventing the Crabtree effect: Replacing media glucose with galactose increases susceptibility of HepG2 cells to mitochondrial toxicants. *Toxicological Sciences*, *97*(2), 539-547.

Meléndez-Hevia, E., Waddell, T. G., & Cascante, M. (1996). The puzzle of the Krebs citric acid cycle: Assembling the pieces of chemically feasible reactions, and opportunism in the design of metabolic pathways during evolution. *Journal of Molecular Evolution*, *43*(3), 293-303.

Moreno-Sánchez, R., Rodríguez-Enríquez, S., Marín-Hernández, A., & Saavedra, E. (2007). Energy metabolism in tumor cells. *The FEBS Journal*, *274*(6), 1393-1418.

Nakahara, Y., Imanishi, S., Mitsumasu, K., Kanamori, Y., Iwata, K.I., Watanabe, M., Kikawada, T. & Okuda, T., (2010). Cells from an anhydrobiotic chironomid survive almost complete desiccation. *Cryobiology*, *60*(2), 138-146.

Parkinson, J. (2002). An essay on the shaking palsy. *The Journal of Neuropsychiatry and Clinical Neurosciences*, *14*(2), 223-236.

Patra, K. C., & Hay, N. (2014). The pentose phosphate pathway and cancer. *Trends in Biochemical Sciences*, *39*(8), 347-354.

Pittelli, M., Formentini, L., Faraco, G., Lapucci, A., Rapizzi, E., Cialdai, F., Romano, G., Moneti, G., Moroni, F. & Chiarugi, A., (2010). Inhibition of nicotinamide phosphoribosyltransferase: Cellular bioenergetics reveals a mitochondrial insensitive NAD pool. *Journal of Biological Chemistry*, *285*(44), 34106-34114.

Placzek, G. (1959). *The Rayleigh and Raman Scattering* (Vol. 526). Lawrence Radiation Laboratory.

Polymeropoulos, M.H., Lavedan, C., Leroy, E., Ide, S.E., Dehejia, A., Dutra, A., Pike, B., Root, H., Rubenstein, J., Boyer, R. & Stenroos, E.S., (1997). Mutation in the α-synuclein gene identified in families with Parkinson's disease. *Science*, *276*(5321), 2045-2047.

Reitzer, L. J., Wice, B. M., & Kennel, D. (1979). Evidence that glutamine, not sugar, is the major energy source for cultured HeLa cells. *Journal of Biological Chemistry, 254*(8), 2669-2676.

Ricci, C., Vaghi, L., & Manzini, M. L. (1987). Desiccation of rotifers (*Macrotrachela quadricornifera*): Survival and reproduction. *Ecology*, *68*(5), 1488-1494.

Robert, B. (2009). Resonance Raman spectroscopy. *Photosynthesis Research*, *101*(2), 147-155.

Rossignol, R., Gilkerson, R., Aggeler, R., Yamagata, K., Remington, S. J., & Capaldi, R. A. (2004). Energy substrate modulates mitochondrial structure and oxidative capacity in cancer cells. *Cancer Research*, *64*(3), 985-993.

Saragusty, J., & Loi, P. (2019). Exploring dry storage as an alternative biobanking strategy inspired by Nature. *Theriogenology*, *126*, 17-27.

Sasic, S., & Ozaki, Y. (Eds.). (2011). *Raman, Infrared, and Near-infrared Chemical Imaging*. John Wiley & Sons.

Schapira, A. V. (1993). Mitochondrial complex I deficiency in Parkinson's disease. *Advances in Neurology*, *60*, 288-291.

Scherer, W. F., Syverton, J. T., & Gey, G. O. (1953). Studies on the propagation in vitro of poliomyelitis viruses: IV. Viral multiplication in a stable strain of human malignant epithelial cells (strain HeLa) derived from an epidermoid carcinoma of the cervix. *The Journal of Experimental Medicine*, *97*(5), 695-710.

Scott, K. L., Lecak, J., & Acker, J. P. (2005). Biopreservation of red blood cells: Past, present, and future. *Transfusion Medicine Reviews*, *19*(2), 127-142.

Shah, M., Rajagopalan, S., Xu, L., Voshavar, C., Shurubor, Y., Beal, F., Andersen, J.K. & Dutta, A.K., (2014). The high-affinity D2/D3 agonist D512 protects PC 12 cells from 6-OHDA-induced apoptotic cell death and rescues dopaminergic neurons in the MPTP mouse model of Parkinson's disease. *Journal of Neurochemistry*, *131*(1), 74-85.

Sharon, M. A., Kozarova, A., Clegg, J. S., Vacratsis, P. O., & Warner, A. H. (2009). Characterization of a group 1 late embryogenesis abundant protein in encysted embryos of the brine shrimp *Artemia franciscana*. *Biochemistry and Cell Biology*, *87*(2), 415-430.

Shih, M. D., Hoekstra, F. A., & Hsing, Y. I. C. (2008). Late embryogenesis abundant proteins. *Advances in Botanical Research*, *48*, 211-255.

Shimizu, T., Kanamori, Y., Furuki, T., Kikawada, T., Okuda, T., Takahashi, T., Mihara, H. & Sakurai, M., (2010). Desiccation-induced structuralization and glass formation of group 3 late embryogenesis abundant protein model peptides. *Biochemistry*, *49*(6), 1093-1104.

Skolik, R. A., Solocinski, J., Konkle, M. E., Chakraborty, N., & Menze, M. A. (2021). Global changes to HepG2 cell metabolism in response to galactose treatment. *American Journal of Physiology-Cell Physiology, 320*(5), 778-793.

Smith, C.A., O'Maille, G., Want, E.J., Qin, C., Trauger, S.A., Brandon, T.R., Custodio, D.E., Abagyan, R. & Siuzdak, G., (2005). METLIN: A metabolite mass spectral database. *Therapeutic Drug Monitoring*, *27*(6), 747-751.

Smith, E., & Morowitz, H. J. (2004). Universality in intermediary metabolism. *Proceedings of the National Academy of Sciences*, *101*(36), 13168-13173.

Smith, R. L., Soeters, M. R., Wüst, R. C., & Houtkooper, R. H. (2018). Metabolic flexibility as an adaptation to energy resources and requirements in health and disease. *Endocrine Reviews*, *39*(4), 489-517.

Soldatow, V. Y., LeCluyse, E. L., Griffith, L. G., & Rusyn, I. (2013). In vitro models for liver toxicity testing. *Toxicology Research*, *2*(1), 23-39.

Solocinski, J., Osgood, Q. A., Rosiek, E., Underwood, L., Zikanov, O., & Chakraborty, N. (2018). Development of a surface tension mediated technique for dry stabilization of mammalian cells. *PloS ONE*, *13*(3), e0193160.

Sparkman, O. D. (2000). *Mass Spectrometry Desk Reference*. Global View Publishing.

Sparkman, O. D., Kitson, F. G., & Penton, Z. E. (2011). *Gas Chromatography and Mass Spectrometry: A Practical Guide*. Elsevier.

Stiles, P. L., Dieringer, J. A., Shah, N. C., & Van Duyne, R. P. (2008). Surface-enhanced Raman spectroscopy. *Annual Review of Analytical Chemistry*, *1*, 601-626.

Sun, F., Dai, C., Xie, J., & Hu, X. (2012). Biochemical issues in estimation of cytosolic free NAD/NADH ratio. *PloS ONE*, *7*(5), e34525.

Tahrani, A. A., Barnett, A. H., & Bailey, C. J. (2013). SGLT inhibitors in management of diabetes. *The Lancet Diabetes & Endocrinology*, *1*(2), 140-151.

Tanaka, M., & Young, R. J. (2006). Review Polarised Raman spectroscopy for the study of molecular orientation distributions in polymers. *Journal of Materials Science*, *41*(3), 963-991.

Taylor, M. J. (2007). Biology of cell survival in the cold: The basis for biopreservation of tissues and organs. In J. G. Baust & J. M. Baust (Eds.), *Advances in Biopreservation* (pp. 15–62). CRC Press.

Tischler, M. E., Friedrichs, D., Coll, K., & Williamson, J. R. (1977). Pyridine nucleotide distributions and enzyme mass action ratios in hepatocytes from fed and starved rats. *Archives of Biochemistry and Biophysics*, *184*(1), 222-236.

Titov, D. V., Cracan, V., Goodman, R. P., Peng, J., Grabarek, Z., & Mootha, V. K. (2016). Complementation of mitochondrial electron transport chain by manipulation of the NAD+/NADH ratio. *Science*, *352*(6282), 231-235.

Tolleter, D., Hincha, D. K., & Macherel, D. (2010). A mitochondrial late embryogenesis abundant protein stabilizes model membranes in the dry state. *Biochimica et Biophysica Acta (BBA)-Biomembranes*, *1798*(10), 1926-1933.

Tolleter, D., Jaquinod, M., Mangavel, C., Passirani, C., Saulnier, P., Manon, S., Teyssier, E., Payet, N., Avelange-Macherel, M.H. & Macherel, D., (2007). Structure and function of a mitochondrial late embryogenesis abundant protein are revealed by desiccation. *The Plant Cell*, *19*(5), 1580-1589.

Tolosa, L., Gómez-Lechón, M. J., Pérez-Cataldo, G., Castell, J. V., & Donato, M. T. (2013). HepG2 cells simultaneously expressing five P450 enzymes for the screening of hepatotoxicity: Identification of bioactivable drugs and the potential mechanism of toxicity involved. *Archives of Toxicology*, *87*(6), 1115-1127.

Vander Heiden, M. G., & DeBerardinis, R. J. (2017). Understanding the intersections between metabolism and cancer biology. *Cell*, *168*(4), 657-669.

Vander Heiden, M. G., Cantley, L. C., & Thompson, C. B. (2009). Understanding the Warburg effect: The metabolic requirements of cell proliferation. S*cience*, *324*(5930), 1029-1033.

Warburg, O. (1956). On respiratory impairment in cancer cells. *Science*, *124*, 269-270.

Warburg, O. (1956). On the origin of cancer cells. *Science*, *123*(3191), 309-314.

Wilkinson, G. R. (2005). Drug metabolism and variability among patients in drug response. *New England Journal of Medicine*, *352*(21), 2211-2221.

Williamson, D. H., Lund, P., & Krebs, H. A. (1967). The redox state of free nicotinamide-adenine dinucleotide in the cytoplasm and mitochondria of rat liver. *Biochemical Journal*, *103*(2), 514.

Wold, S., Esbensen, K., & Geladi, P. (1987). Principal component analysis. *Chemometrics and Intelligent Laboratory Systems*, *2*(1-3), 37-52.

Wong, C. H., Siah, K. W., & Lo, A. W. (2019). Estimation of clinical trial success rates and related parameters. *Biostatistics*, *20*(2), 273-286.

Wouters, O. J., McKee, M., & Luyten, J. (2020). Estimated research and development investment needed to bring a new medicine to market, 2009-2018. *JAMA*, *323*(9), 844-853.

Xu, D., Duan, X., Wang, B., Hong, B., Ho, T. H. D., & Wu, R. (1996). Expression of a late embryogenesis abundant protein gene, HVA1, from barley confers tolerance to water deficit and salt stress in transgenic rice. *Plant Physiology*, *110*(1), 249-257.

Yang, H., Yang, T., Baur, J.A., Perez, E., Matsui, T., Carmona, J.J., Lamming, D.W., Souza-Pinto, N.C., Bohr, V.A., Rosenzweig, A. & de Cabo, R., (2007). Nutrient-sensitive mitochondrial NAD+ levels dictate cell survival. *Cell*, *130*(6), 1095-1107.